Univerzita Karlova v Praze
Matematicko–fyzikální fakulta

DIPLOMOVÁ PRÁCE

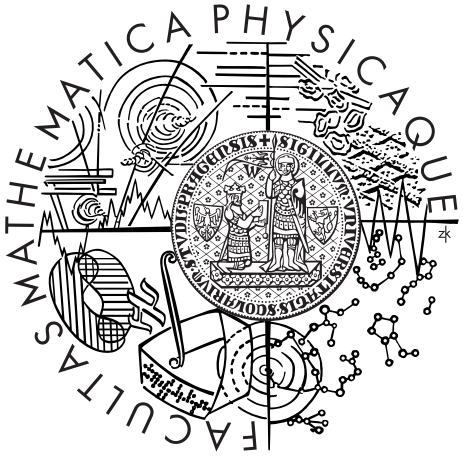

Stanislav Štefánik

Studium urychlování vysokoenergetických částic v extragalaktických objektech

Ústav částicové a jaderné fyziky

Vedoucí diplomové práce: RNDr. Dalibor Nosek, Dr.
Studijní program: Fyzika
Studijní obor: Jaderná a subjaderná fyzika

Praha 2013

Charles University in Prague
Faculty of Mathematics and Physics

MASTER THESIS

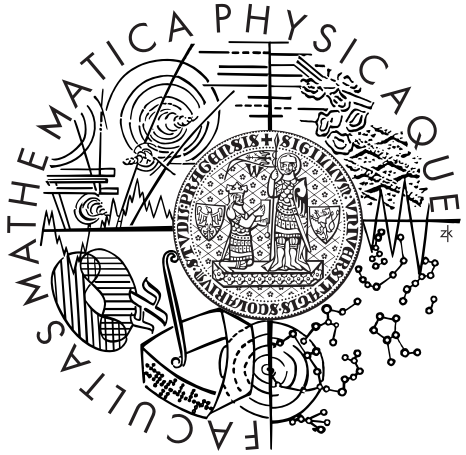

Stanislav Štefánik

Study of Cosmic–Ray Acceleration in Extragalactic Objects

Institute of Particle and Nuclear Physics

Supervisor of the master thesis: RNDr. Dalibor Nosek, Dr.
Study programme: Physics
Specialization: Nuclear and Subnuclear Physics

Prague 2013

Acknowledgements

Rád by som sa poďakoval svojmu školiteľovi RNDr. Daliborovi Noskovi, Dr. za jeho veľkú pomoc a ochotu pri výbere mojej diplomovej práce. Veľmi si vážim jeho cenné rady a priateľský prístup počas konzultácií.

Taktiež ďakujem mojim rodičom a bratom za ich stálu podporu nielen v priebehu písania diplomovej práce, ale i počas celého doterajšieho štúdia.

I declare that I carried out this master thesis independently, and only with the cited sources, literature and other professional sources.

I understand that my work relates to the rights and obligations under the Act No. 121/2000 Coll., the Copyright Act, as amended, in particular the fact that the Charles University in Prague has the right to conclude a license agreement on the use of this work as a school work pursuant to Section 60 paragraph 1 of the Copyright Act.

In Prague signature of the author

Názov práce:	Studium urychlování vysokoenergetických částic v extragalaktických objektech
Autor:	Stanislav Štefánik
Katedra:	Ústav částicové a jaderné fyziky
Vedúci diplomovej práce:	RNDr. Dalibor Nosek, Dr.

Abstrakt: Práca sa zaoberá spôsobmi produkcie kozmického γ–žiarenia v astrofyzikálnych objektoch a metódami jeho detekcie. V súvislosti s danou problematikou sú diskutované možné interakcie produkujúce γ–žiarenie v aktívnej galaxii Centaurus A. Predstavený je nový experiment Cherenkov Telescope Array zameraný na detekciu atmosférických spŕšok iniciovaných kozmickým γ–žiarením. Prostredníctvom simulácií atmosférických spŕšok programom CORSIKA je študované Čerenkovovo žiarenie emitované v ich priebehu. Popísaná je analýza dát v rámci experimentov využívajúcich Čerenkovovské teleskopy a jej aplikácia na súbor dát z aktívnej galaxie PKS 2155-304. Výsledkom analýzy je štatistické testovanie na prítomnosť zdroja γ–žiarenia a jeho časovej premennosti.

Kľúčové slová: Kozmické žiarenie, gama, žiarenie, astročasticová fyzika, urýchľovanie, experiment CTA

Title:	Study of Cosmic–Ray Acceleration in Extragalactic Objects
Author:	Stanislav Štefánik
Department:	Institute of Particle and Nuclear Physics
Supervisor:	RNDr. Dalibor Nosek, Dr.

Abstract: This thesis deals with production processes of cosmic γ–rays in astrophysical objects and methods of their detection. Possible interactions leading to the emission of high energy γ–rays in the active galaxy Centaurus A are discussed in this context. Cherenkov Telescope Array is presented as a new experiment focused on the detection of air showers initiated by cosmic γ–rays. Cherenkov light of air showers is studied in the simulations done by CORSIKA simulation tool. Method of data analysis within the framework of Cherenkov telescopes is described and performed on the dataset of the active galaxy PKS 2155-304. The results include statistical tests of γ–ray source presence and its time variability.

Keywords: Cosmic rays, gamma rays, astroparticle physics, high energy astrophysics, acceleration, CTA experiment

Contents

Introduction

This thesis deals with the physics of cosmic rays in extragalactic sources. Since charged particles in cosmic rays are subjects to multiple deflections in magnetic fields, they are not suitable for direct observations of their sources. Detection of neutral secondary products of cosmic ray interactions is the most effective way of the study of production and acceleration scenarios of cosmic rays . Thus, interest is especially paid to the cosmic γ–rays in this work. In particular, simulations of γ–rays and the study of production processes are aimed at the very high energy (VHE) range. This is done because current and future ground based experiments working in this regime are the most successful ones in the observations of low γ–ray fluxes up to the energies of 10^{15} eV.

The purpose of Chapter 1 is to deliver basic information about the cosmic rays and its γ–component. The physics of plausible acceleration mechanisms of cosmic ray particles is discussed. Production processes of γ–radiation in astrophysical environments are described.

Chapter 2 deals with imaging atmospheric Cherenkov telescope arrays (IACTs) which made a significant breakthrough in γ–astronomy during the last decade. Observations of cosmic γ–rays by these experiments rely on the detection of Cherenkov radiation produced in air showers initiated by the cosmic rays. Therefore a substantial part of Chapter 2 is devoted to the simulations of air showers induced by charged particles and γ–rays. I simulated Cherenkov light production in air showers, as well. Distributions of Cherenkov radiation on the ground are studied for different initial conditions.

Second part of Chapter 2 is aimed at the analysis methods used by IACTs. As an illustration, I determined significance of observed signal from the extragalactic source PKS 2155-304. Along with that, I performed statistical test for time variability of γ–ray sources on the dataset from PKS 2155-304.

Cherenkov Telescope Array (CTA) is presented in Chapter 3 as a new promising IACT experiment. Description of its crucial parameters along with comparison of its performance with previous telescope arrays are given.

I studied the nearest active galaxy Centaurus A in detail in Chapter 3. Emphasis is put on possible production processes of VHE γ–radiation in this source. Results obtained by various experiments are cited. I discussed the role of CTA instrument in the context of improvement of the current knowledge about this active galactic nucleus and production processes of γ–rays.

1. Cosmic ray physics

The purpose of this chapter is to discuss basic properties of cosmic rays and their acceleration. Section 1.1 deals with the observed spectrum and peculiar nature of cosmic rays, regarding its unknown origin and acceleration. Fermi acceleration is described in Section 1.2 as a promising mechanism of production of cosmic rays with highest energies.

The emphasis is in this Chapter put on the γ–radiation of astrophysical origin, since it essentially carries indirect information about the primary cosmic rays from which it descends. Production mechanisms of cosmic γ–rays are described in Section 1.3 as a prerequisite for discussion of γ–ray production in the nearest active galactic nucleus Centaurus A, see Chapter 3.

1.1 Cosmic rays in general

The phenomenon of cosmic rays remains not well understood even after a century since its discovery by Hess [28]. A brief description of known properties as well as unsolved problems regarding cosmic rays is given in the following.

The term 'cosmic rays' is usually denoted for charged particles of astrophysical origin. The composition of cosmic rays is dominated by protons ($\sim 85\%$) and in lesser amount by helium ($\sim 12\%$) and heavier nuclei ($\leqslant 1\%$) [40]. Electrons comprise only a fraction (2%) of all cosmic rays.

Energy spectrum of cosmic rays is shown in Fig.1.1. It can be effectively described by a power–law function which is a hint that cosmic ray particles are of non-thermal origin, i.e. they have to be produced in other environments than conventional sources of thermal radiation (e.g. stars). Intensity of particles above several GeV and below some 100 TeV is given by [40]

$$I(E) \approx 1.8 \times 10^4 E^{-\Gamma} \mathrm{m}^{-2}\ \mathrm{s}^{-1}\ \mathrm{sr}^{-1}\ \mathrm{GeV}^{-1}, \tag{1.1}$$

where the spectral index in the given energy range is $\Gamma = 2.7$.

Two distinctive features are present in the energy spectrum of cosmic rays. Firstly, the spectral break around 10^{15} eV, so called 'knee', causes the spectrum to steepen at higher energies with spectral index Γ approximately equal to 3.1 [40]. The common belief is that cosmic rays below the knee are produced inside our Galaxy [9] [52]. Particles with energies above the knee are thought to be primarily of extragalactic origin but it is not clear whether some portion of them does not originate within the Galaxy.

Supernova remnants (SNRs) are considered to be major contributors to the galactic cosmic rays [9]. One reasons for that is the enormous amount of energy released in supernovae explosions which is some two orders of magnitude higher than energy stored in galactic cosmic rays [41]. Thus, SNRs alone are capable of sustaining the observed flux of cosmic rays in our Galaxy. Another fact supporting the hypothesis of the origin of cosmic rays in SNRs is the possibility of particle acceleration in shock fronts caused by supernovae explosions. So far, this has been the most plausible mechanism of cosmic ray acceleration up to the knee, see Section 1.2.

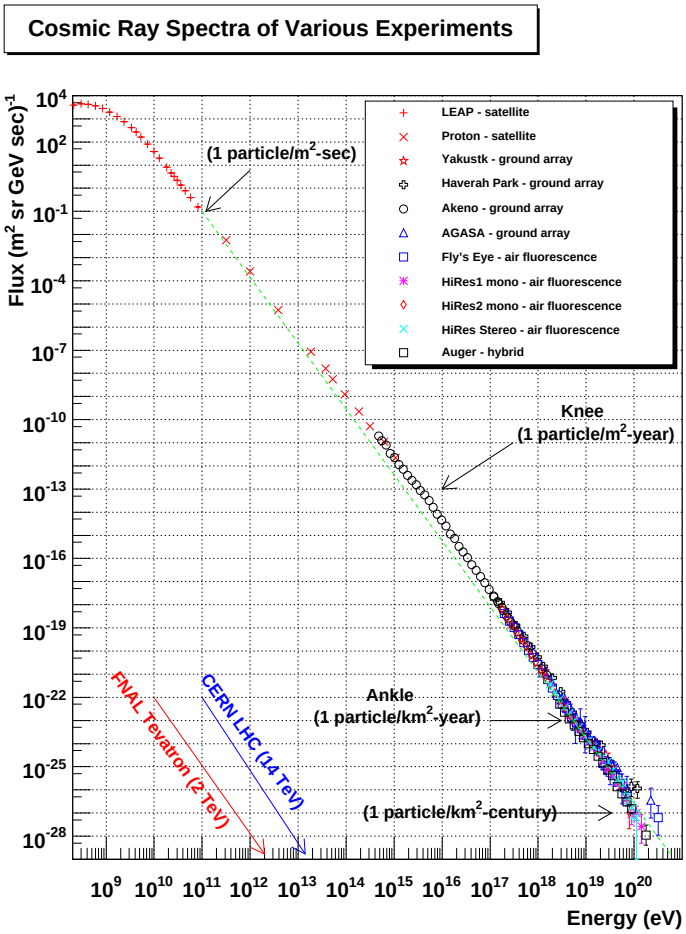

Figure 1.1: Energy spectrum of cosmic rays as measured by various experiments. Shown is the flux of particles of given energy per unit area, solid angle and time. Taken from Hanlon [25].

The second feature in the energy spectrum is the 'ankle' at about 10^{18} eV where the spectrum becomes flatter. Particles with energies above the ankle are believed to originate in extragalactic sources [52]. It is explained by so called Hillas condition [29] for minimum size of sources and strength of their magnetic fields. Cosmic rays need to be confined within the considered acceleration region for a sufficient amount of time in order to achieve very high energies. Magnetic fields of astrophysical objects force charged particles to stay inside the region as long as the gyroradii of particles are smaller than sizes of the regions. Hence, there exists a correspondence between the size of the source region L (given in parsecs[1)]) and its magnetic field strength B (given in microgauss) [29]

$$\left(\frac{B}{\mu\mathrm{G}}\right)\left(\frac{L}{\mathrm{pc}}\right) > \left(\frac{E}{10^{15}\mathrm{eV}}\right)\frac{1}{Z\beta}, \tag{1.2}$$

[1)] 1 pc $= 3.09 \times 10^{16}$ m

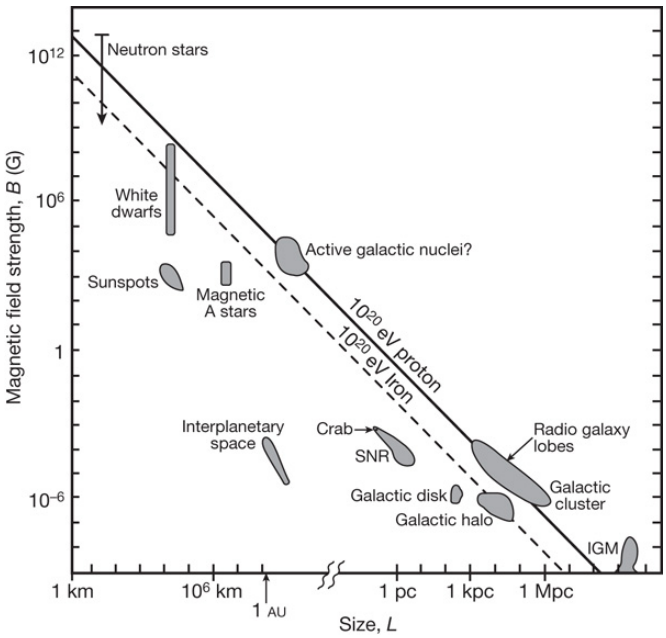

Figure 1.2: Hillas diagram showing requirements for the minimum sizes and magnetic fields of astrophysical objects needed to accelerate particles to given energies. A source is considered capable of this accelaration, if it is located above the line corresponding to specific energy of given particle. Taken from Bauleo & Rodríguez Martino [17].

where Z is the charge of a particle and β denotes the speed of a shock wave, see Section 1.2. Fig.1.2 shows potential cosmic ray sources according to minimum values of size and magnetic field strength of an object. To date, no astrophysical objects were confirmed as sources of cosmic rays with ultra–high energies above 10^{18} eV.

1.2 Fermi acceleration

Theory of cosmic ray acceleration to very high energies can be described by Fermi mechanisms. An acceleration of particles in magnetized clouds of interstellar matter proposed by Fermi [23] is explained here.

Let v_c be the velocity of a cloud moving at non-relativistic speed. Cosmic ray particles with energies E_0 collide with this cloud at some angle θ relative to its velocity vector. Particles are exposed to the influence of the magnetic field inside the cloud. As a result, their directions are changed many times and finally they escape the cloud with new energy E_1. The exit angle θ_1 of particles relative to the movement of the cloud which is generally different from θ. Energies of particles in the rest frame (marked with an asterisk) of the cloud are given by

$$E_0^* = \gamma_c E_0 (1 - \beta_c \cos\theta_0), \tag{1.3}$$

where $\beta_c = v_c/c$ and $\gamma_c = (1-\beta_c^2)^{-\frac{1}{2}}$. Equality $E_0^* = E_1^*$ is valid in the rest frame of the cloud, since interactions of particles inside the cloud are considered to be

ideally elastic. The escape energy is equal to

$$E_1 = \gamma_c E_0^*(1 + \beta_c \cos\theta_1^*). \tag{1.4}$$

Relative energy gain of particles as a result of encounter with the cloud is given as

$$\frac{\Delta E}{E} = \frac{E_1 - E_0}{E_0} = \gamma_c^2(1 - \beta_c \cos\theta_0)(1 + \beta_c \cos\theta_1^*) - 1 \equiv \xi. \tag{1.5}$$

Particles escape the cloud isotropically, i.e. $\langle \cos\theta_1^* \rangle = 0$, due to the multiple random scattering inside the cloud. Therefore, positive gain of energy happens when the condition $\theta \in (\pi/2, 3\pi/2)$ is satisfied. These 'head-on' collisions are statistically more probable than collisions at other angles [42].

Probability of interaction between cosmic ray particle and the cloud is proportional to difference between their velocities $(v - v_c \cos\theta_0)$. Probability density is therefore given by [35]

$$\frac{\mathrm{d}n}{\mathrm{d}\Omega_0} \propto (1 - \beta_c \cos\theta_0). \tag{1.6}$$

Averaging over all values of θ_0 one gets the value of $\langle \cos\theta_0 \rangle$:

$$\langle \cos\theta_0 \rangle = \frac{\int \cos\theta_0 \frac{\mathrm{d}n}{\mathrm{d}\Omega_0} \mathrm{d}\Omega_0}{\int \frac{\mathrm{d}n}{\mathrm{d}\Omega_0} \mathrm{d}\Omega_0} = -\frac{\beta_c}{3}. \tag{1.7}$$

Assuming $\langle \cos\theta_1^* \rangle = 0$ and inserting Eq.(1.7) along with the definition of Lorentz factor in the Eq.(1.5) one gets

$$\langle \xi \rangle = \frac{1 + \frac{\beta_c^2}{3}}{1 - \beta_c^2} - 1 \simeq \frac{4}{3}\beta_c^2. \tag{1.8}$$

Hence the energy gain is proportional to the square of cloud's speed which gives rise to the name of this type of acceleration, i.e. *second order Fermi acceleration.*

Since the partial energy gain is the same throughout the acceleration process, the energy of particle after n interactions with the cloud is equal to [35]

$$E_n = E_0(1 + \xi)^n. \tag{1.9}$$

where the number of encounters n necessary for acquiring given energy E_n is

$$n = \ln\left(\frac{E_n}{E_0}\right) / \ln(1 + \xi). \tag{1.10}$$

Particles can escape the cloud during each encounter with the probability P. Assuming that the energies of particles remain unchanged after escape from the cloud, the probability of gaining energy E_n is $(1 - P)^n$. The number of particles with energies higher than E_n is proportional to the number of particles which underwent the acceleration in the cloud more than n–times. With the use of Eq.(1.10) one gets [24]

$$\begin{aligned} N(> E_n) &= N_0 \sum_{k=n}^{\infty} (1 - P)^k = N_0 \sum_{k=0}^{\infty} (1 - P)^k - N_0 \sum_{k=0}^{n} (1 - P)^k \\ &= N_0 \frac{1}{1 - (1 - P)} - N_0 \frac{1 - (1 - P)^n}{1 - (1 - P)} \\ &= \frac{N_0}{P}(1 - P)^{\ln(\frac{E_n}{E_0})/\ln(1+\xi)} \propto \frac{N_0}{P}\left(\frac{E_n}{E_0}\right)^{-\gamma}, \end{aligned} \tag{1.11}$$

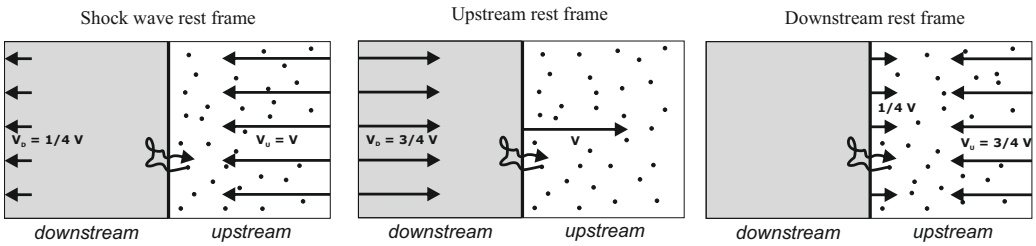

Figure 1.3: Acceleration of comic ray particles in shock fronts.

where $\gamma \simeq P/\xi$.

It is evident that second order Fermi acceleration is consistent with the power–law form of energy spectrum of cosmic rays. However, it does not account for the correct value of the spectral index [41]. The energy gain is β^2–dependent which together with small values of β means that this acceleration model is not sufficient to explain the observed energies of cosmic ray particles.

First order Fermi acceleration was proposed as a more efficient way of accelerating cosmic ray particles to the observed energies [16], [18]. According to this model, particles are accelerated in the shock waves, e.g. from supernovae explosions. Shock waves are created due to very rapid expansion of material from supernova remnants, velocity of which exceeds the speed of sound in the ambient medium.

Shock wave disturbs the material in front of it (upstream region). Velocity of the shock wave is equal to $v \simeq 4v_{\rm D}/3$, where $v_{\rm D}$ is the velocity of the medium behind the shock front (downstream region), see Fig.1.3. Interstellar gas in front of the perturbation moves at the speed v relative to the shock wave in its rest frame. Downstream material moves away from the shock front with the velocity $v/4$. In the downstream rest frame, the shock wave moves away with the speed $v/4$ while the upstream material collides with the downstream region at the speed $3v/4$.

Cosmic ray particles in the interstellar medium cross the discontinuity from the upstream region to the region behind the shock front and vice versa. These crossings can be repeated many times and the particles always undergo 'head-on' collisions with the shock wave. Therefore, unlike the encounters of particles with magnetized clouds, particles always gain energy after passing through the shock fronts. Energy gain of particles after one crossing is $\xi \sim 4\beta/3$, where β denotes the difference between velocities of the shock wave and the material behind it [35]. Discussion leading to Eq.(1.11) is the same in the case of first order Fermi acceleration. Acceleration in shock waves reproduces the power–law spectrum of cosmic rays and it si moreover linear in β. Hence, it is possible to explain cosmic ray spectrum along with its index by this mechanism.

Maximum energy of particles obtainable during acceleration in shock fronts can be estimated as [37]

$$E_{\rm max} = 5 \times 10^6 Z \left(\frac{B}{10^{-5}\ {\rm G}} \right)\ {\rm GeV}, \tag{1.12}$$

where B stands for the magnetic field strength.

Table 1.1: Energy domains of γ–ray astronomy. Taken from Aharonian [9].

Domain	Energy interval
low (LE)	$\leqslant 30$ MeV
high (HE)	30 MeV – 30 GeV
very high (VHE)	30 GeV – 30 TeV
ultra high (UHE)	30 TeV – 30 PeV
extremely high (EHE)	$\geqslant 30$ PeV

1.3 Gamma radiation component of cosmic rays

Charged cosmic ray particles are deflected by magnetic fields present in the source regions and interstellar magnetized clouds (Section 1.2), not to mention the magnetic field of the Earth. Randomization of arrival directions of cosmic rays with energies $< 10^{18}$ eV is a major obstacle in the detection of sources and in the study of acceleration scenarios.

On the other hand, γ–rays generated in the interactions of cosmic rays with ambient gases, radiation and magnetic fields propagate directly from the source region towards the observer. As they are secondary products, they carry only indirect information about primary cosmic rays. Nevertheless, observations of γ–radiation can pinpoint the source regions and restrict their sizes. In some cases it is also possible to differentiate between hadronic and leptonic origin of γ–ray emission. Moreover, detection of cosmic γ–rays is successfully performed by ground based experiments, see Section 2.3 and Chapter 3. Because of these arguments, γ–ray astronomy is important means of gathering knowledge about extreme processes in which cosmic rays are produced and accelerated.

Energy spectra of cosmic γ–rays are usually divided into several bands according to the energy of considered radiation [9]. Such division is adopted also in this work and it is specified along with used abbreviations in Table 1.1.

VHE γ–observations performed by imaging atmospheric Cherenkov telescopes in the last decade significantly contributed to the detection of new sources of cosmic rays. VHE γ–rays were detected from supernova remnants and their shells. Other galactic sources were observed for the first time in VHE–regime as well, e.g. pulsars, pulsar wind nebulae and binary stellar systems. Detected extragalactic sources include starburst galaxies and nuclei and jets of active radio galaxies which are often considered to be the candidate birthplace of the highest energetic particles ever observed, see Section 3.3. Other potential sources of VHE γ–radiation, which are yet to be confirmed or dismissed, are star clusters, galaxy clusters and molecular clouds.

1.3.1 Production processes of γ–rays

There are many different scenarios of γ–ray production in astrophysical environments. Their overview is given in the following. Division of these processes according to the type of parent cosmic ray particles is adopted here, i.e. leptonic or hadronic origin of γ–radiation.

Leptonic processes

- **Inverse Compton scattering:** Interactions of electrons with interstellar radiation fields can lead to the inverse Compton (IC) scattering. These fields include starlight, cosmic microwave background (CMB), infrared background light and synchrotron radiation from electrons. Inverse Compton scattering is one of the most important production processes of VHE γ–rays, since it has high efficiency of γ–ray production over the whole energy spectrum. This is because of CMB filling up the entire universe and also because of low density of targets contributing to other competitive mechanisms, i.e. interstellar gas and magnetic fields [9].

  Let $E_{\rm e}$ and ω_γ be the energies of electron and target photon, respectively. The cross–section for IC scattering approaches classical Thompson cross–section $\sigma_{\rm T}$ in the non–relativistic approximation, i.e. for $E_{\rm e}\omega_\gamma \ll 1$ [40]:

$$\sigma_{\rm IC} \approx \sigma_{\rm T}\left(1 - 2E_{\rm e}\omega_\gamma\right). \tag{1.13}$$

  The cross–section in ultra–relativistic region ($E_{\rm e}\omega_\gamma \gg 1$) is given by the simplified Klein–Nishina formula:

$$\sigma_{\rm IC} \approx \frac{3\sigma_{\rm T}}{8E_{\rm e}\omega_\gamma}\ln\left(4E_{\rm e}\omega_\gamma\right). \tag{1.14}$$

  Assuming monoenergetic fields of photons with energy ω_γ and density n_γ, energy loss rates for Thomson (non–relativistic) and Klein–Nishina (relativistic) regime, respectively, are given by [9]

$$\begin{aligned}\left(\frac{{\rm d}E_{\rm e}}{{\rm d}t}\right)_{\rm IC} &= -\frac{4}{3}\sigma_{\rm T}c\omega_\gamma n_\gamma E_{\rm e}^2 && \text{Thomson}\\ \left(\frac{{\rm d}E_{\rm e}}{{\rm d}t}\right)_{\rm IC} &= -\frac{3}{8}\frac{\sigma_{\rm T}cn_\gamma}{\omega_\gamma}\left[\ln\left(4E_{\rm e}\omega_\gamma\right) - \frac{11}{6}\right] && {\rm Klein-Nishina}\end{aligned} \tag{1.15}$$

  The cooling time of electrons due to Thomson scattering is [9]

$$t_{\rm IC} \approx 3\times 10^8\left(\frac{u_\gamma}{1\ {\rm eV\ cm^{-3}}}\right)^{-1}\left(\frac{E_{\rm e}}{1\ {\rm GeV}}\right)^{-1}\ {\rm yr}, \tag{1.16}$$

  where u_γ denotes the energy density of target photon field.

- **Synchrotron radiation:** Electrons exposed to the magnetic fields move along curved trajectories and subsequently emit electromagnetic radiation. Energies of these synchrotron photons are generally much lower than those of parent electrons. Hence the cosmic ray electrons do not contribute significantly to the VHE γ–rays through synchrotron radiation. On the other hand, synchrotron photons are major constituents of radio emission from our Galaxy, SNRs and extragalactic radio sources [40]. Synchrotron radiation also contributes to the optical and X-ray emission from SNRs and active radio galaxies.

  Average energy losses of electrons due to the synchrotron radiation are given effectively by the same equation as in the case of IC scattering in

non–relativistic regime, i.e. the first line in the Eq.(1.15). Consequently, synchrotron cooling time of electrons is the same as in Eq.(1.16) apart from the change $u_\gamma \to B^2/8\pi$, where B denotes the magnetic field strength.

- **Bremsstrahlung:** Bremsstrahlung is an interaction of charged particles with matter, particularly with electromagnetic fields of atoms in ambient gas. Cosmic ray electrons lose their energy with the average loss rate [9]

$$\left(\frac{\mathrm{d}E_\mathrm{e}}{\mathrm{d}t}\right)_\mathrm{brems} = -\frac{m_\mathrm{p} c n E_\mathrm{e}}{X_0}, \tag{1.17}$$

where n stands for the gas density in given medium and X_0 is the radiation length[2)]. With the use of Eq.(1.17) one gets for electron cooling time due to the bremsstrahlung [9]:

$$t_\mathrm{brems} = \frac{E_\mathrm{e}}{-\mathrm{d}E_\mathrm{e}/\mathrm{d}t} \approx 4 \times 10^7 \left(\frac{n}{1\ \mathrm{cm}^{-3}}\right)^{-1}\ \mathrm{yr}. \tag{1.18}$$

Comparing Eq.(1.18) with combined cooling time due to the IC scattering and the synchrotron radiation one finds out that the latter two processes prevail against the bremsstrahlung on condition that [9]

$$E_\mathrm{e} \geqslant 10 \left(\frac{u_\gamma + B^2/8\pi}{1\ \mathrm{eV\ cm}^{-3}}\right)^{-1} \left(\frac{n}{1\ \mathrm{cm}^{-3}}\right)\ \mathrm{GeV}. \tag{1.19}$$

- **Electron–positron annihilation:** Annihilation of $e^- e^+$ pairs is another way of γ–ray production via interactions of matter. The total cross–section of annihilation of a relativistic positron with energy E_e is equal to [9]

$$\sigma_\mathrm{ann} = \frac{3}{8}\frac{m_\mathrm{e} c^2}{E_\mathrm{e}} \sigma_\mathrm{T}^2 \left[\ln\left(2\frac{E_\mathrm{e}}{m_\mathrm{e} c^2}\right)\right]. \tag{1.20}$$

Cooling time due to the annihilation is given by [9]

$$t_\mathrm{ann} = 4 \times 10^6 \frac{E_\mathrm{e}}{m_\mathrm{e} c^2} \frac{1}{\ln\left(2\frac{E_\mathrm{e}}{m_\mathrm{e} c^2}\right) - 1} \left(\frac{n}{1\ \mathrm{cm}^{-3}}\right)^{-1}\ \mathrm{yr}. \tag{1.21}$$

It follows from Eqs.(1.18) and (1.21) that energy losses due to the annihilation are higher than those due to the bremsstrahlung at positron energies less than 15 MeV. Thus, annihilation of $e^- e^+$ does not play significant role in γ–ray production in the VHE region.

Hadronic processes

- π^0 **decays:** One of the most important hadronic interaction leading to the production of VHE γ–rays are inelastic collisions of protons and nuclei in cosmic rays with the interstellar gas, particularly pp–interactions. Among

[2)] $X_0 = 7/9(n\sigma_0)^{-1}$, where σ_0 is the bremsstrahlung cross–section. Thus, radiation length is the average distance over which electrons lose all their energy except for the fraction $1/e$ due to the bremsstrahlung. Alternatively, it is the same as the mean free path of γ–rays.

other particles, all three types of π–mesons are also produced in these collisions with roughly equal probabilities. Subsequent decays $\pi^0 \rightarrow 2\gamma$ and $\pi^{\pm}$ into ν_{e}, ν_{μ} (and corresponding antineutrinos) result in similar spectra of final particles. Thus γ–ray astronomy can be linked with observations of cosmic ray neutrinos and provide some predictions for neutrino fluxes.

The total cross section for inelastic collisions of protons is given as [9]

$$\sigma_{\mathrm{pp}} \approx 30 \left[0.95 + 0.06 \ln \left(\frac{E_{\mathrm{kin}}}{1 \text{ GeV}} \right) \right] \text{ mb}. \tag{1.22}$$

For kinetic energies of protons $E_{\mathrm{kin}} \leqslant 1$ GeV $\sigma_{\mathrm{pp}} = 0$ is assumed. This approximation does not significantly change fluxes of γ–rays at lower energies. Cooling time of protons due to the inelastic *pp*–collisons in hydrogen-filled medium with number density n_{H} can be estimated as [9]

$$t_{\mathrm{pp}} = \frac{1}{n_{\mathrm{H}} \sigma_{\mathrm{pp}} f c} \simeq 5.3 \times 10^7 \left(\frac{n}{1 \text{ cm}^{-3}} \right)^{-1} \text{ yr}, \tag{1.23}$$

where $f \approx 0.5$ denotes the inelasticity coefficient and the average value $\sigma_{\mathrm{pp}} \approx 40$ mb was assumed.

Since t_{pp} is energy independent above the energy of 1 GeV, spectrum of γ–rays from π^0–decays reproduces the initial spectrum of cosmic ray protons. It follows from this finding that the detection of VHE γ–rays can be effectively exploited to gather indirect information about the origin of cosmic rays.

- **Inverse Compton scattering:** Scattering of protons in the radiation fields is effectively the same process as the IC scattering of electrons. However, the average energy loss in the hadronic IC scattering is for given energies of electrons and protons smaller than in the case of the leptonic scattering by a factor of $(m_{\mathrm{e}}/m_{\mathrm{p}})^4 \approx 10^{-13}$ [9]. Therefore the IC scattering of protons is not a relevant way of γ–ray production in the astrophysical environments.

- **Photomeson production:** Production of γ–rays from π^0–mesons can apart from *pp*–collisions proceed via interactions of protons or nuclei with radiation fields, i.e.

$$p + \gamma \rightarrow p + k\pi^0, \tag{1.24}$$

where k denotes multiplication of the final–state pions in the case of high energies of primary protons. Threshold energy for these processes is approximately 140 MeV [9].

- **Synchrotron radiation:** The cooling time of protons due to the synchrotron radiation is

$$t_{\mathrm{synch}} = 4.5 \times 10^4 \left(\frac{B}{100 \text{ G}} \right)^{-2} \left(\frac{E}{10^{19} \text{ eV}} \right)^{-2} \text{ s}. \tag{1.25}$$

Synchrotron radiation of protons is regarded as an inefficient way of γ–ray production unless specific circumstances occur. In extreme astrophysical

environments, where cosmic rays can be accelerated up to the ultra–high energies of 10^{20} eV and above, synchrotron cooling time of protons can be of the same order of magnitude, or even less, than cooling times of other competing hadronic processes. Thus, some of the VHE γ–rays can originate as synchrotron radiation of UHECRs.

2. Air showers and Cherenkov technique of detection

Since the energy spectrum of cosmic rays and its gamma component follow a power law [40], it is necessary to carry out measurements of γ–ray fluxes with energies higher than several tens of GeV on large area scales. This requirement rules out space satellite experiments and we are thus left with indirect ground based measurements. Such gamma astronomy observations exploit the fact that incident cosmic photons interact at the top of the atmosphere and produce cascades of particles, mainly electrons, positrons and other photons [9]. Secondary charged particles move at relativistic speeds and are able to produce Cherenkov radiation along their motion through the atmosphere.

Because of its importance in γ–ray observations, this chapter is devoted to problematics of formation and detection of Cherenkov light of air showers. Basic insight into the physics of air showers and their Cherenkov radiation is given in Section 2.1. Results of air shower simulations using CORSIKA program are presented throughout Section 2.2. Differences of various simulated air showers as a result of change in initial conditions, e.g. energy of primary particles, observation level height and zenith angle of air showers are discussed in Sections 2.2.4, 2.2.5 and 2.2.6, respectively.

Of vital importance is the description and subsequent comparison of electromagnetic and hadronic air showers, see Section 2.2.2. This is because of its usefulness in background rejection in Cherenkov light image analysis, which is described in Section 2.3 along with stereoscopic method of gamma ray detection.

A method for testing γ–ray flux time variability is described in Section 2.3.3. Results of its application are given for several recently observed sources.

2.1 Cherenkov light

When approaching the outer layers of the Earth's atmosphere the primary cosmic rays interact with gas molecules and give birth to new, secondary particles. The usual height of initial interaction is approximately 20–25 km above the sea level [9]. Because of high energies of primaries, secondary particles possess enough energy to again produce new particles, thus creating an air shower.

In case of photon induced showers, the driving interactions for production of particles are e^-e^+ pair production and bremsstrahlung, see Chapter 1. This processes have effectively two–particle character in the final state. Cosmic ray protons and nuclei interact through hadronic interactions with nuclei of air, leading to creation of bunches of new particles, unlike the previous case. These include nucleons, all types of pions, hyperons and both charged and neutral leptons. Neutral pions rapidly π^0 decay almost exclusively into two photons, which in turn contribute to electromagnetic cascade. In fact, substantial part of primary hadron energy is transformed into electromagnetic subshower. However, this differs from γ–ray shower because of greater lateral displacement of hadronic shower, see Section 2.2.2.

Development of an air shower continues to the height of about 8–10 km where

it reaches its maximum. From this point the ionization losses outweigh to other types of processes. Particles already do not have enough energy to create new ones and the shower dies out in the upper atmosphere. Only secondary particles from air showers with energies of several TeV and above can reach the ground and be detected at mountain altitudes of around 2000 m [9]. Energy of primary particles is fully deposited throughout the atmosphere, which effectively acts as an calorimeter. While this is true for electromagnetic showers, hadronic showers produce significant number of muons and neutrinos through decays of charged pions. These are able to reach the ground and this can pose troubles with false triggering of Cherenkov telescopes in the case of muons.

Direct observations of secondary charged particles prove unsuccessful in case of smaller shower energies. However, these species can be also detected due to observation of electromagnetic radiation they produce. Relativistic particles can emit so called Cherenkov radiation, provided that their velocity is higher than actual phase velocity of light in given medium, $v_{\mathrm{ph}} = c/n$, n being refractive index. Putting this condition into the expression for Lorentz gamma factor one arrives at estimate of minimum energy needed for production of Cherenkov radiation by relativistic particle:

$$E_{\mathrm{min}} = \frac{mc^2}{\sqrt{1 - n^{-2}}}. \tag{2.1}$$

This requirement is easily met by most of secondaries which therefore emit Cherenkov light into the cone with apex angle equal to

$$\theta = \arccos\left(\frac{1}{n\beta}\right), \tag{2.2}$$

which is approximately 1° at shower maximum. As a result, particles at shower maximum altitude ~ 10 km generate a pool of Cherenkov photons with radius $\sim$ 130 m on the ground.

Because of height dependence of air refractive index, the angle of the cone is somewhat smaller for altitudes above shower maximum and greater (up to $\sim 1.5^\circ$) below this maximum [30]. Therefore, a Cherenkov ring of mentioned radius is formed for particles at and above the maximum which can be seen in Fig.2.1 on the left. The ring of roughly 280 m in diameter is clearly visible here. In this case smeared dots represent mainly photons emitted by charged particles deflected further from shower axis due to Coulomb scattering. On the other hand, lower emitted Cherenkov photons have to travel smaller distances and arrive closer to the shower axis, though the cone apex angle is larger for them. Therefore, the ring is no more recognized in the right image of Fig.2.1, depicting distribution of photons on the ground produced below the shower maximum. Images shown in Fig.2.1 where created using CORSIKA air shower simulation program [26] described in Section 2.2.1.

2.2 Morphology of air showers

In order to analyse data from Cherenkov detectors and to plan new experiments, development and properties of air showers have to be well known. These are studied by the means of Monte Carlo simulations and therefore substantial part

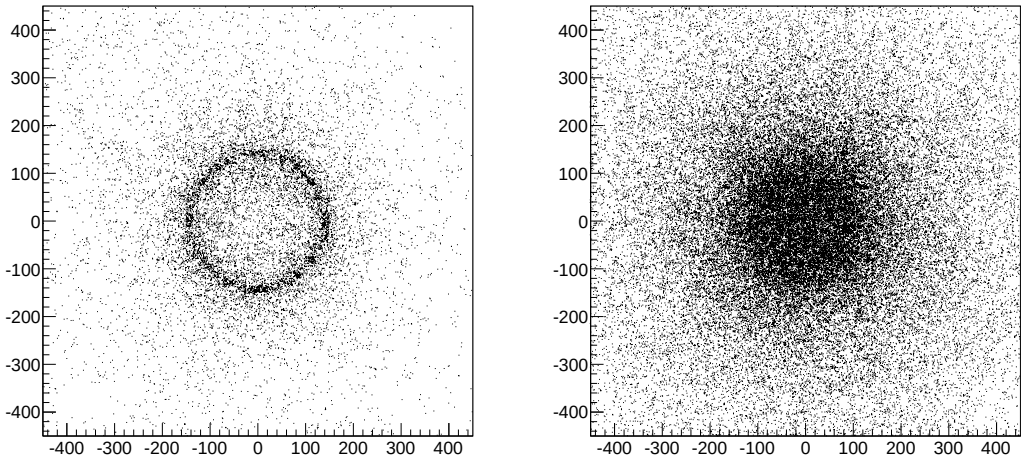

Figure 2.1: Left: Ground level image of Cherenkov photons produced in the height of 10 km and above in 1 TeV γ–induced shower. Right: The same for Cherenkov photons emitted below the height of 7 km. Positions (in metres) of Cherenkov photon bunches from CORSIKA output were plotted adopting shower impact point as centre of coordinate system. Grid of 3600 Cherenkov detectors with spacing 15 m was simulated for photon detection.

of this chapter is devoted to them. In this work, emphasis is put on dependencies of Cherenkov light distribution on energy of primary particles (Section 2.2.4), height of observation level (Section 2.2.5) and zenith angle of incoming particles (Section 2.2.6). Apart from that, differences between air showers initiated by γ–rays, protons and electrons are studied (Sections 2.2.2 and 2.2.3).

2.2.1 CORSIKA as an air shower simulation tool

All following simulations of air showers were performed using program CORSIKA (COsmic Ray SImulations for KAscade, [26]) which was developed for the KASCADE [2] experiment in Karlsruhe. It is a Monte Carlo based tool used to study development of air showers by simulation of interactions which arise during their expansion. These include collisions and decays of nuclei, hadrons, electrons, positrons, photons and muons. CORSIKA can simulate air showers up to $\sim 10^{20}$ eV of primary particle's energy. Since Cherenkov arrays operate in the range $\sim 10\ \mathrm{GeV} - 100\ \mathrm{TeV}$, all simulations in this work are restricted within this energy interval.

Various primary conditions can be defined in CORSIKA input files. For the purpose of this Chapter, performed variations are those of particle's type, their primary energy, angle of incidence and the observation altitude. Output from program regarding particles in air showers contains among other data information on type of particles, their momenta, positions and arrival times to the observation level measured from first interaction.

High–energy hadronic interactions can be simulated by various models within CORSIKA. In this work QGSJET-II-03 model (Quark Gluon String model with

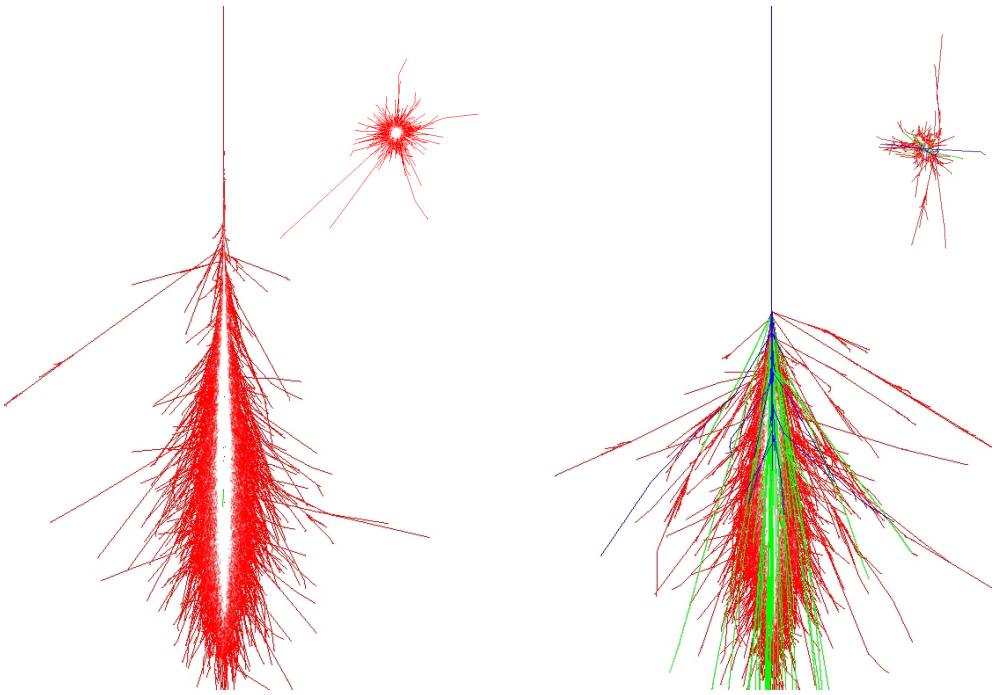

Figure 2.2: Particle tracks for 1 TeV gamma (left) and proton (right) air shower. Selected views are in the $x-z$ (vertical) and $x-y$ direction (horizontal, in corners), z being vertical axis parallel to air shower axis. Colours illustrate different components of shower, red standing for electromagnetic, blue for hadronic and green for muonic part. Images were obtained using Plot option in CORSIKA.

JETs) was used. It utilises quark gluon string model for treatment of hadronic processes [27].

Apart from simulations of extensive air showers, Cherenkov light production during shower development can be simulated via Cherenkov option in CORSIKA. Cherenkov radiation is collected only within areas of Cherenkov detectors, since computation space and time are not sufficient enough to manage the very large amount of photons produced in showers. Detectors can be predefined in Cherenkov option of CORSIKA with desirable diameters in a rectangular grid of variable spacings between them. Alternatively, Cherenkov light can be detected by the means of imaging atmospheric Cherenkov telescopes (see Section 2.3) simulated via IACT option in CORSIKA and subsequent use of the `sim_telarray` program [20]. This was however performed here only for the purpose of Fig.2.18. Cherenkov output files contain number of photons in particular bunches (maximum value of photons treated together as a single bunch can be predefined in CORSIKA input file), positions of Cherenkov bunches, their arrival time since the first interaction and the height of bunch production.

2.2.2 Electromagnetic and hadronic showers

Shower events caused by protons and nuclei in cosmic rays constitute to dominant background when observing γ–rays using ground based experiments. The aim of this section is therefore the analysis of differences between electromagnetic

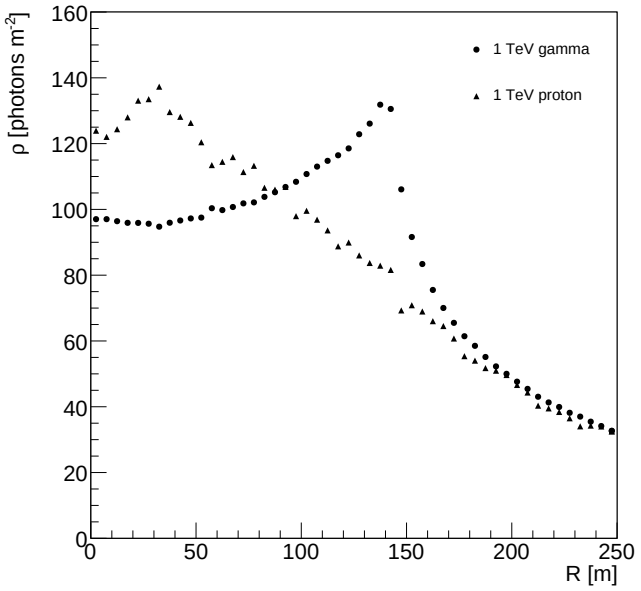

Figure 2.3: Lateral distribution of Cherenkov light density at sea level. Primary particles were 1 TeV γ–ray and proton. Detector of dimension of 5×500 meters centred in the shower impact point was adopted. The size and position of detector was chosen such that the radial distribution of Cherenkov radiation could be acquired but, at the same time, the computation time and data size were kept in reasonable limits.

and hadronic showers, in particular their longitudinal and lateral development. The former group comprises showers caused by cosmic ray photons, electrons or positrons but only γ–rays are taken into account here, since $e^{\pm}$–initiated showers have effectively the same structure (see Section 2.2.3). As an example of hadronic showers only proton–initiated showers are considered because protons form the bulk ($\sim 90\%$, Longair [40]) of cosmic rays.

In both bremsstrahlung and pair production final particles are produced in forward direction, meaning that angles between their and primary particle's trajectories are small. As a result of that, electromagnetic shower is collimated around its axis unlike showers from cosmic ray nuclei which generally acquire greater lateral displacement because of hadronic interactions. This difference between the two types of showers is of great importance in the analysis of Cherenkov light images where so called reduced parameters are used to describe each detected shower. Shower distributions in reduced width and length of images (see Section 2.3.1) take on very distinctive character due to different lateral spread. Therefore, proper selection of events according to these distributions allows effective rejection of background caused by cosmic ray nuclei, see Section 2.3.1. For comparison, 1 TeV gamma and proton–initiated showers were simulated and plotted in $x - y$ and $x - z$ direction in Fig.2.2.

The most energetic particles contribute to the thin Cherenkov ring of given radius. Therefore one can expect the greatest density of Cherenkov photons from electromagnetic showers in a distance from axis equal to the ring radius after

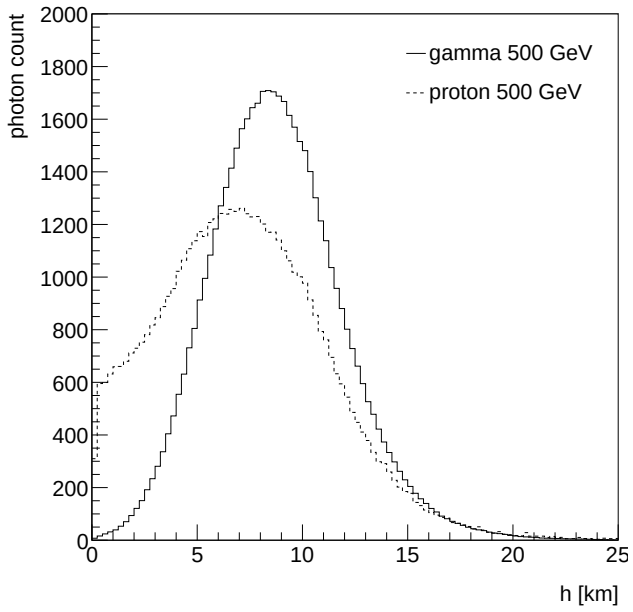

Figure 2.4: Longitudinal distributions of produced Cherenkov photons as functions of height above the sea level. Histograms were obtained from simulation sets of 100 showers induced by γ–rays (solid) and protons (dashed) with energy 500 GeV. A grid of 1×1 m detectors with spacing of 15 m was predefined. Radiation was detected in bunches of 5 photons. These conditions were chosen in order to reduce the data from vast number of produced photons to reasonable, yet sufficient amount.

which a rapid decline in density should follow. This is illustrated by simulation of 100 showers initiated by 1 TeV γ–ray. Lateral distribution of Cherenkov photon density was simulated for proton–initiated showers of same energy as well. Both dependencies are plotted in Fig.2.3 showing expected behaviour for γ–showers and featureless distribution for protons.

If only interactions responsible for lateral displacement in electromagnetic showers were bremsstrahlung and pair production, all Cherenkov photons would arrive inside the ring of radius ∼130 m. However, Coulomb scattering of photons causes significant deflection away from shower axis resulting in Cherenkov photons hitting the ground far beyond dimensions of the pool [30]. This scattering is most prominent for lower energy particles. Lateral diffusion caused by Coulomb scattering is given by Molière radius

$$R_{\text{Molière}} \sim r_1 \frac{E_\text{c}}{E} = \frac{E_\text{s}}{E_\text{c}} X_0 \frac{E_\text{c}}{E}, \tag{2.3}$$

r_1 being Molière unit, roughly equal to 9.3 g.cm^{-2}, or 78 m at sea level for low energy particles [24]. E_c is critical energy of particles at shower maximum where ionization losses start to dominate [1)] and $E_\text{s} = \sqrt{\frac{4\pi}{\alpha}} m_\text{e} c^2 \sim 21$ MeV.

Longitudinal distribution of Cherenkov photons is plotted in Fig.2.4 containing histograms showing height dependence of produced radiation. Both electro-

[1)] $E_\text{c} \sim 88$ MeV for electrons [44]

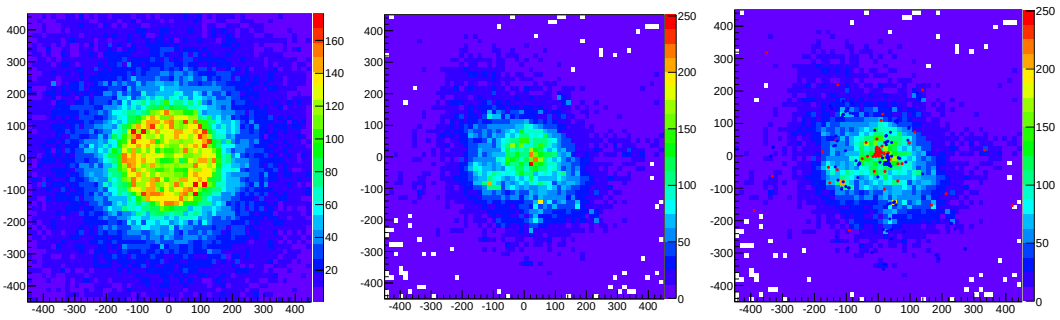

Figure 2.5: Density of Cherenkov photons on the ground as a function of coordinates in the plane orthogonal to shower axis. Histograms were created from CORSIKA simulated showers initiated by 1 TeV photon (left) and proton (centre). Positions of incoming particles from proton–induced shower are marked in the right image, red standing for muons and blue for electrons. Each bin corresponds to the spacing between two neighbouring detectors, i.e. 15×15 metres.

magnetic and hadronic showers exhibit rapid growth but, in case of the latter, the maximum of shower occurs in greater atmospheric depth. Also 'dying' of the hadronic shower is slower, hence more particles are able to reach the ground. These particles are responsible for localized peaks in Cherenkov photon density with $1/r$ dependence [30], r being distance from particle impact point.

Histogram of density on the ground from single showers of electromagnetic and hadronic origin is plotted in Fig.2.5. Coordinates of particles actually hitting the ground are marked by single points in an additional plot. Correlation between position of these particles and areas of higher Cherenkov light intensity is visible in this image.

2.2.3 Electron–initiated showers

Another type of background noise during γ–ray observations are showers caused by cosmic ray electrons or positrons, as they are charged particles interacting with magnetic fields. Differences between γ– and electron–induced showers are discussed in this section.

It may seem that electron–initiated showers cannot be practically recognized from gamma showers. This is true for energies of primary particles above some 100 GeV which corresponds to the energy range of current ground based Cherenkov telescopes. Observations at such high energies have to deal with background noise caused almost exclusively by cosmic ray nuclei, since electron flux is negligible in this case. Looking at energy spectrum of cosmic ray electrons in Fig.2.6 we can see that electron flux is smaller by approximately 3 orders of magnitude than the flux of cosmic ray nuclei. However, when one attempts to detect γ–radiation in range of several tens of GeV, diffuse cosmic electron flux must be taken into account [49]. Hadronic background does not play significant role here because higher energies of primary nuclei are needed in order to produce comparable amount of Cherenkov light as in γ–initiated shower. In fact, it is not possible to observe hadronic showers below ~ 50 GeV.

Discrepancies between electron and γ–showers become more prominent in this

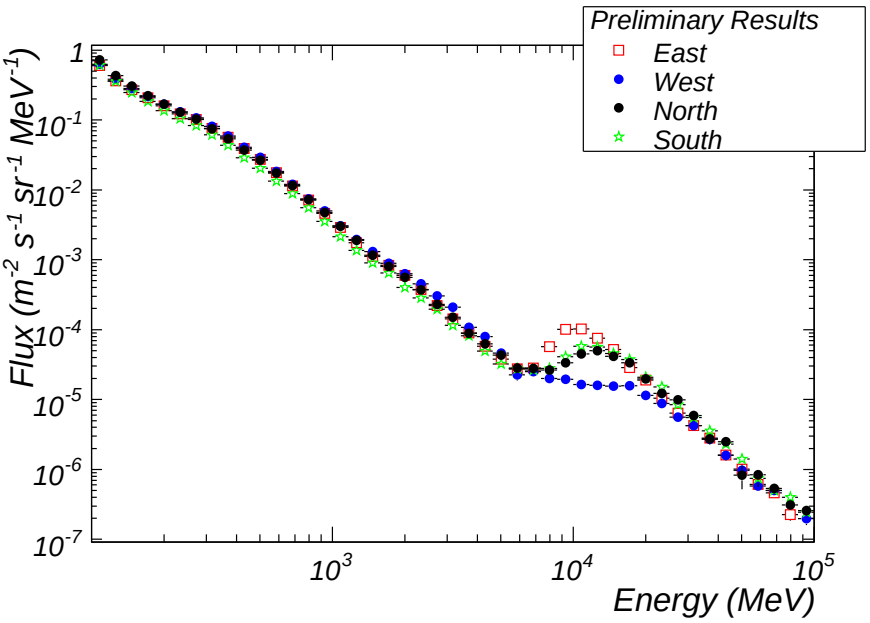

Figure 2.6: Energy spectrum of cosmic ray electrons as measured by Fermi collaboration [46].

low energy regime with more intense electron flux. Interaction length of primary electrons is noticeably smaller than that of photons. Therefore, maximum of electron–induced showers occurs at higher altitudes. For the atmospheric depth of shower maximum an approximating relation can be derived [49]:

$$X^{\gamma,\mathrm{e}}_{\mathrm{max}}(E) = 1.01 X_0 \left[\ln \frac{E}{E_\mathrm{c}} - n \right], \quad n = \begin{cases} 1 & \text{photons} \\ 0 & \text{electrons} \end{cases} \tag{2.4}$$

Here E_c stands for critical energy and X_0 is the radiation length in the air. Difference $\Delta(E)$ between shower heights of both types of particles is given by

$$\Delta(E) \simeq \frac{h_\mathrm{s}}{2\left(\ln \frac{E}{E_\mathrm{c}} - 1\right)}, \tag{2.5}$$

where h_s is the scale–height of atmosphere equal to 7.1 km. While for showers generated by primary particles with energy 10 GeV $\Delta(10\ \mathrm{GeV}) \approx 1.14$ km, for primary energy of 100 GeV the difference is about one half of this distance. As a consequence, electron– and γ–initiated showers are indistinguishable at very high energies.

Due to higher altitudes of shower maximum, lateral spread of showers induced by electrons is larger. Thus corresponding Cherenkov photon density at observation level is smaller as can be seen in Fig.2.7. This effectively means that unlike γ–rays, electrons cannot trigger Cherenkov telescope at the same energy. Another difference between both types of electromagnetic shower is Cherenkov photon arrival time. Time pulse of Cherenkov light from showers generated by low energy electrons peaks earlier. It is significantly broader than in the case of photon–induced showers [49]. Fig.2.8 depicts the number of Cherenkov photons as a function of their arrival time.

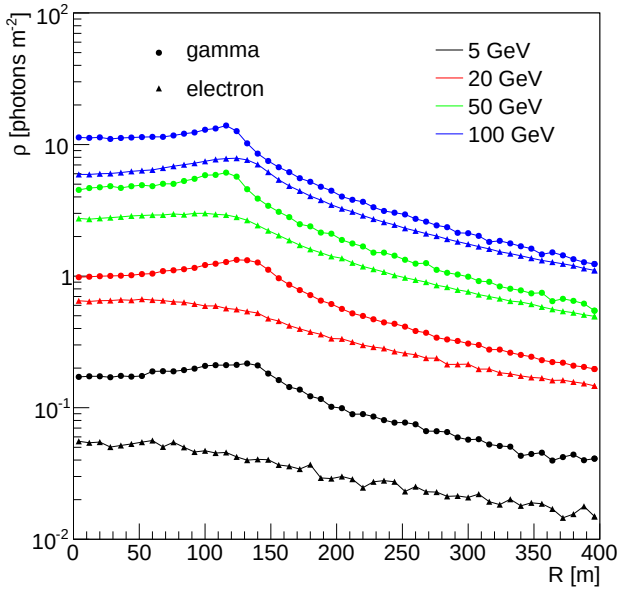

Figure 2.7: Lateral distributions of γ– (circles) and electron– (triangles) initiated showers as a function of their primary energy. Showers of vertical incidence were simulated adopting one Cherenkov detector of size 500 × 5 m in sets of 1000 events.

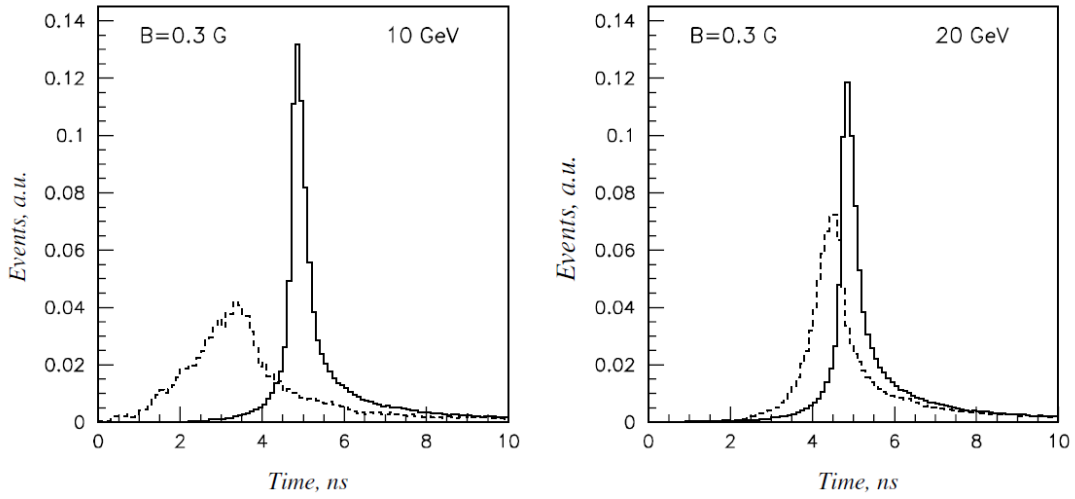

Figure 2.8: Time distribution of Cherenkov pulses. Taken from Sahakian et al. [49].

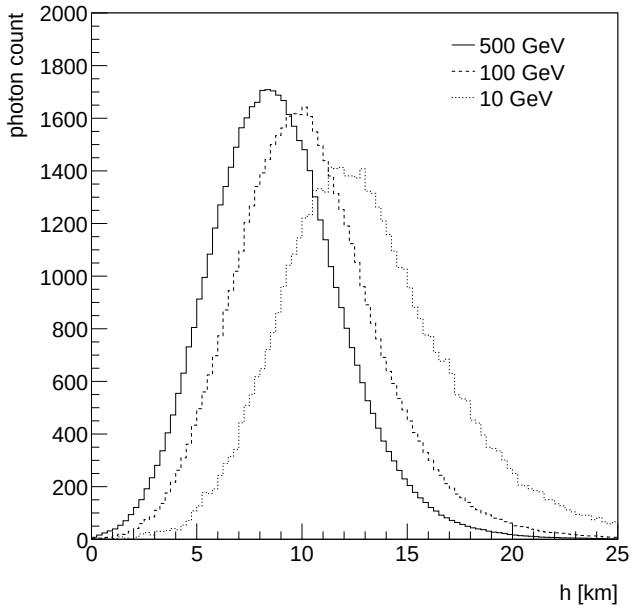

Figure 2.9: Longitudinal distribution of Cherenkov photons from simulated γ–induced showers as a function of their energy.

Longer pulse duration and higher detection threshold in case of electron–initiated showers enable one to separate these species from relevant events triggered by primary γ–rays. It appears that an effective way of rejecting electron–caused background should be proper choice of signal pulse duration [49]. This is the case of new generation of Cherenkov telescopes, i.e. CTA which will extend the operating energy range down to $\sim$ 10 GeV.

2.2.4 Energy dependence of air showers

Current imaging atmospheric Cherenkov telescope arrays (IACT, see Section 2.3) operate from energies of $\sim$ 50 GeV up to $\sim$ 100 TeV (further details on IACTs in Section 3.1). Therefore changes of Cherenkov light distribution for different energies of primary particles are described in this section, along with requirements on telescopes at threshold energies. Attention will be paid only to γ–initiated showers in following discussions, as they are the only relevant means of gathering astrophysical information in given energy range.

High energy limit of an instrument is given by low incoming gamma ray flux at energies above several hundreds of TeV and therefore it is primarily matter of Cherenkov array size. On contrary, low energy threshold of a telescope is the result of its ability to collect enough light photons. This is because with decreasing primary energy fewer particles, that are able to emit Cherenkov radiation, are produced. Moreover, low energy primary particles cannot penetrate as deep in the atmosphere and their shower maximum occurs earlier in the atmosphere. This behaviour can be seen in Fig.2.9 where longitudinal development of Cherenkov light production is shown for three different energies.

Higher altitude of shower maximum has the consequence of lower photon den-

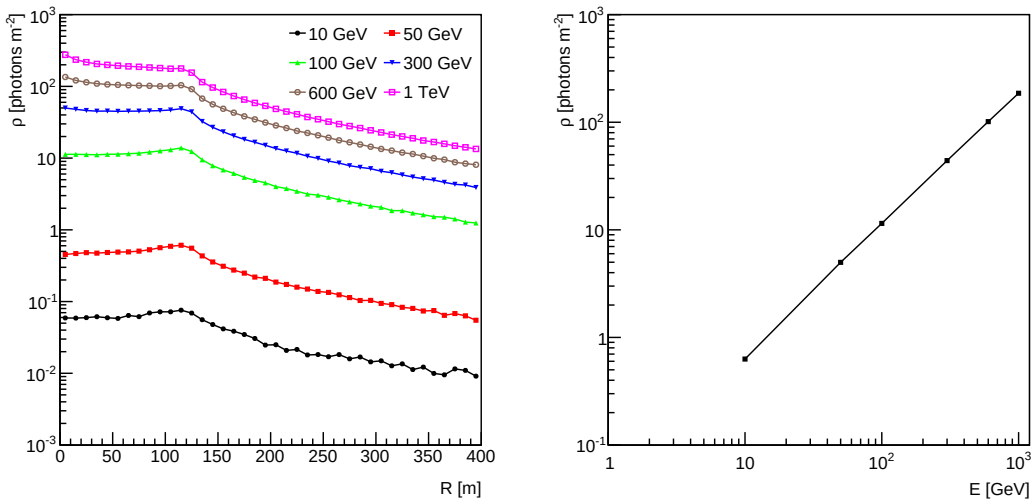

Figure 2.10: Left: Radial dependence of Cherenkov light density plotted for several values of primary γ–ray energy. Right: Average photon density in a circle with radius of 150 m as a function of particle's energy. Data were obtained from sets of simulated showers generated by primary γ–ray of vertical incidence. Observation height was set to the sea level.

sity on the ground. Left panel of Fig.2.10 illustrates this fact by comparing lateral distributions of shower sets with different energies. Average photon density up to the distance of 150 m from shower axis was obtained from these distributions. It is plotted as a function of energy in the right image. It is evident that photon density is linearly increasing with energy.

Different sets of cuts on image parameters are used in Cherenkov image analysis in order to achieve maximum noise rejection and image quality, see Section 2.3.1. Only images with certain amplitude, measured in photoelectrons (p.e.) gained from camera pixels, are allowed in further analysis. For example in H.E.S.S. collaboration [28] a minimum value of 80 p.e. is adopted in standard selection cuts [12]. Number of detected photoelectrons is given by Cherenkov photon density ρ, typically in distance of $\sim$ 100 m from the shower axis, and the telescope photoelectron response [14]

$$A_{\mathrm{p.e.}} = \xi_{\gamma\to\mathrm{e}} A_{\mathrm{mir}}, \tag{2.6}$$

A_{mir} being actual mirror area and $\xi_{\gamma\to\mathrm{e}}$ is the factor describing conversion of photons to photoelectrons. Photoelectron gain can be then estimated as

$$N_{\mathrm{p.e.}} \simeq \rho A_{\mathrm{p.e.}} \tag{2.7}$$

Taking 80 p.e. as detection minimum and using value of Cherenkov photon density from Fig.2.10 in the Eq.(2.7), e.g. $\sim$ 3 photons per m^2 for shower of energy 50 GeV, one gets $A_{\mathrm{p.e.}} \approx 27$ m^2. Usual quantum efficiency of photomultiplier tubes in current telescopes amounts to $\xi_{\gamma\to\mathrm{e}} \sim 0.2 - 0.3$. Thus a telescope of mirror size at least 130 m^2, equivalent to 13 m diameter, would be necessary to detect showers generated by γ–ray of given energy. This is only crude estimate,

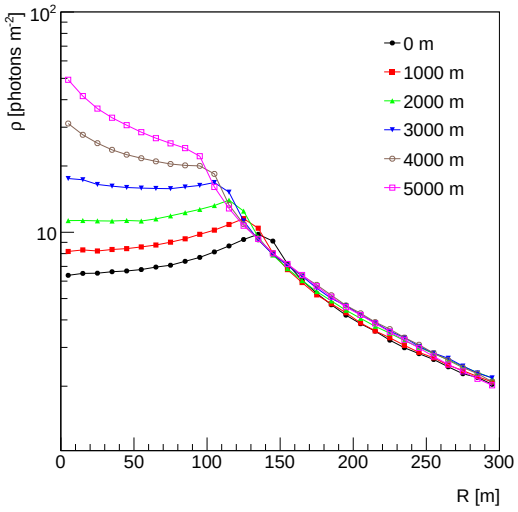

Figure 2.11: Lateral distribution of Cherenkov light as a function of observation altitude. Simulated showers were initiated by 100 GeV γ–rays, vertical incidence was assumed.

since energy threshold depends also on telescope camera pixel size and data acquisition time gate [15]. Actual mirror size could be then larger. On the other hand, observation level height is also very important as at higher altitudes photon density increases. However, already at this stage it is evident that expansion of operative energy range in next generation of IACTs will require large mirror sizes, i.e. several hundreds square metres.

2.2.5 Observation level dependence of air showers

Observing Cherenkov light from air showers at higher altitudes increases the amount of detected photons per given area. This fact results from two basic aspects. First of them is absorption of Cherenkov light in the air. Obviously, less photons are attenuated on smaller distances from production point to observer. However, this was not considered in following simulations.

The other fact affecting the photon density is geometrical layout of shower. Length of Cherenkov ring radius is given by $R_C = (h - h_{obs}) \tan \theta_c$ where h is production height and h_{obs} denotes height of observer. Therefore with increasing altitude the area of Cherenkov pool decreases and corresponding photon density is larger. Fig.2.11 shows this behaviour, containing lateral distribution of Cherenkov light from 1000 showers as a function of height above sea level. Distinctive peak in distributions is shifted towards the shower axis due to smaller Cherenkov ring radius. At higher observation levels this peak is less noticeable when compared to distances closer to the axis. Reason for that is higher concentration of particles capable of Cherenkov emission in this area.

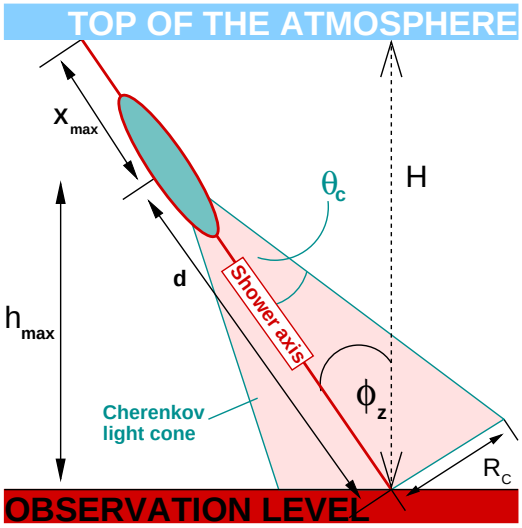

Figure 2.12: Geometry of Cherenkov emission in an air shower with non–zero zenith angle ϕ_z. X_{max} is distance travelled by particle before reaching shower maximum and h_{max} is height of this maximum measured from observation level. Distance from maximum to the shower impact point on the ground is denoted as d. The image was taken from Berge [19].

2.2.6 Zenith angle dependence of air showers

So far, only vertical incidence of primary particles was assumed in simulations, i.e. zero zenith angle. However, most γ–ray observations are carried out with non–zero inclination angle, hence it is important to analyse Cherenkov light production under different zenith angles.

Geometrical layout of important quantities in an air shower inclined under zenith angle ϕ_z is drawn in Fig.2.12. From this picture an approximate expression for Cherenkov cone radius on the ground can be derived. Firstly, height of shower maximum is given by

$$h_{max} = H - X_{max} \cos \phi_z. \tag{2.8}$$

Here X_{max} is distance traveled by particle before reaching shower maximum and H stands for height of the atmosphere. Secondly, distance between shower maximum and impact point is equal to

$$d = \frac{h_{max}}{\cos \phi_z} = \frac{H}{\cos \phi_z} - X_{max}. \tag{2.9}$$

Putting this expression into the relation for Cherenkov ring radius $R_C = d \tan \theta_c$, θ_c being Cherenkov cone opening angle, and taking $\tan \theta_c \approx \theta_c$, we arrive at

$$R_C \simeq \left(\frac{H}{\cos \phi_z} - X_{max} \right) \theta_c. \tag{2.10}$$

When observing γ–initiated showers it is important to consider Cherenkov detector's effective area A_{eff}. This is the area over which is the detector sensitive to incoming events and is roughly given by the size of Cherenkov light pool [42],

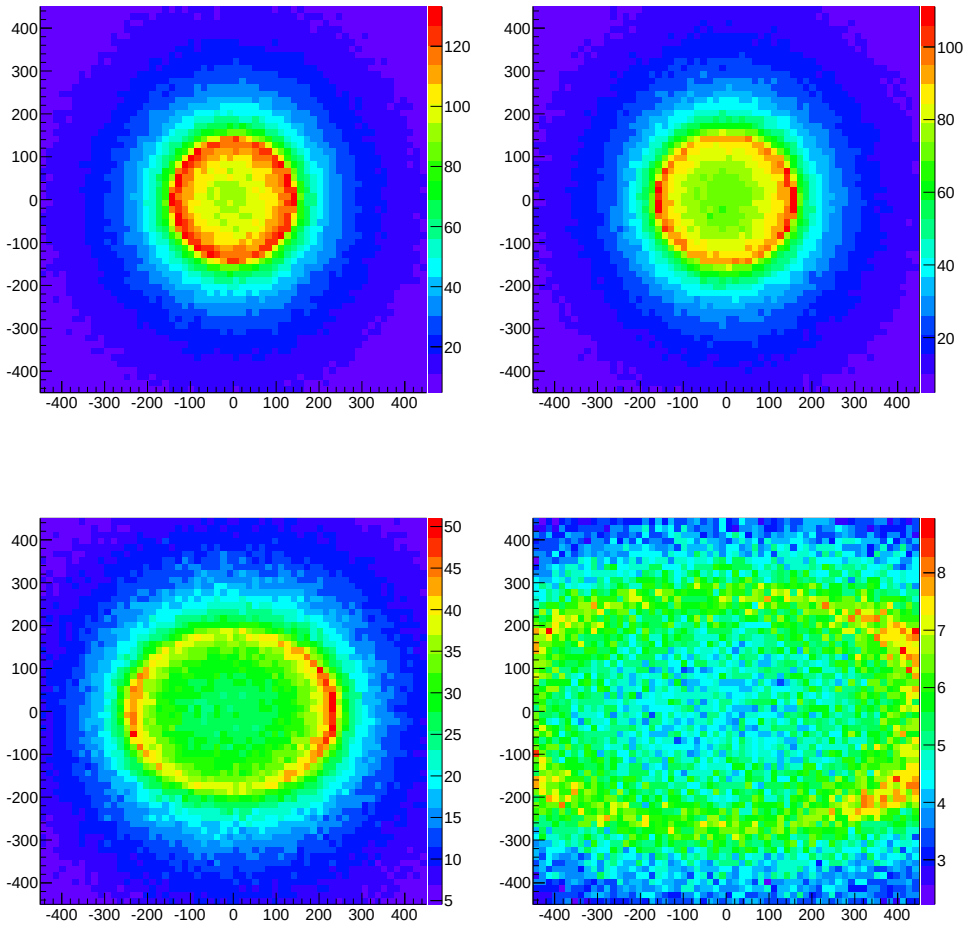

Figure 2.13: Zenith angle dependence of Cherenkov photon density on ground level. From top left clockwise: 0°, 20°, 60°, 40°. Primary particles of 100 simulated showers were 1 TeV γ–rays. For Cherenkov light detection a rectangular grid of 1 m^2 detectors was simulated with spacing of 15 metres. Azimuth angle of impacting particles was set to zero in entire shower set in order to see elongation of the ring for large zenith angles.

i.e.

$$A_{\text{eff}} \approx \pi \left(\frac{R_{\text{C}}}{\cos \phi_{\text{z}}} \right)^2 . \tag{2.11}$$

It follows from this relation that effective area of an instrument is larger for increasing zenith angles. On the other hand, intensity of Cherenkov light within the pool is decreasing function of zenith angle as can be seen from Fig.2.13. Density of Cherenkov photons on the ground was illustrated here by means of 2D histograms for different values of incident angle. Light from more inclined showers is distributed across larger area than in case of nearly vertical incidence. Hence corresponding photon density is lower as can also be seen in Fig.2.14 containing lateral distributions as functions of zenith angle. Zenith angle dependence of average photon density inside the circle of 150 m radius is plotted in the right panel. Data points were fitted assuming that $\rho \sim A^{-2}$ and exploiting Eq.(2.11).

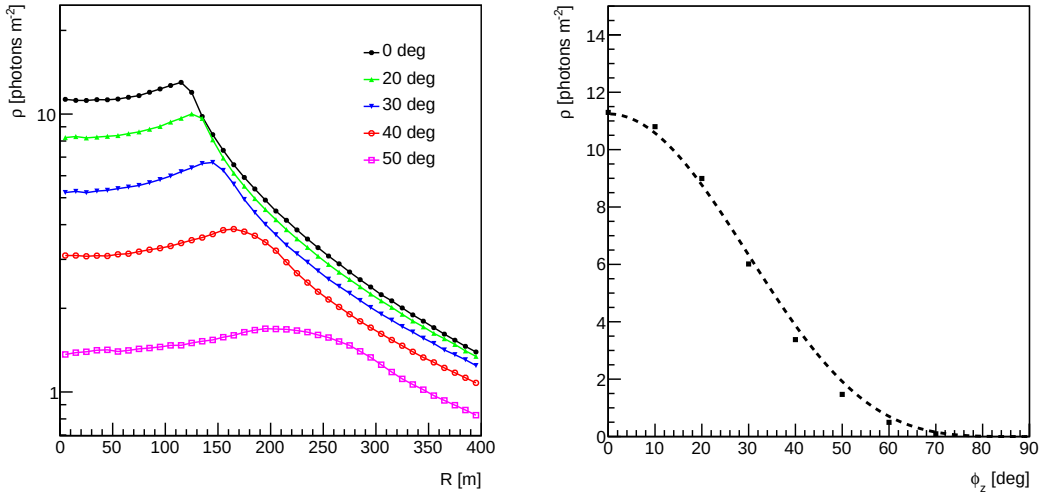

Figure 2.14: Left: Lateral distribution of 1000 γ–initiated showers for several values of zenith angles. Energy of primary particles is 100 GeV in all cases, observation level height is 2000 m a.s.l. Right: Zenith angle dependence of average photon density in 150 m circle (squares). Dashed line represents fit to this data set: $\rho = 11.3 \cos^4 \phi_z$. Azimuth angle of incoming particles was taken from interval $(-180°, 180°)$, as to obtain symmetrical radial distribution.

Large effective area is important for achieving good sensitivity of telescope array which is effectively equal to lowest observable flux[2)]. Therefore large zenith angles are desirable but one must take into account decreasing photon density here. Assuming 100 m^2 telescope mirror area, photon–to–photoelectron conversion efficiency $\xi_{\gamma\to e} \sim 0.2$ and demanding at least 80 p.e. image amplitude we get approximately 3.7 photons per square metre as minimum value of photon density needed for detection. Equation $\rho = 11.3 \cos^4 \phi_z$ was obtained from fit of Fig.2.14. Inserting value for minimum photon density into this equation one arrives at $\phi'_{z,max} \simeq 41°$ as maximum zenith angle allowed for observation. Observation level was set to 2000 m a.s.l. in these simulations , since most of Cherenkov array experiments run at mountain altitudes, see Section 3.1.

Mentioned mirror size is similar to Phase I–telescopes of the H.E.S.S. project. Therefore we can link energy corresponding to the minimum photon density value with H.E.S.S. threshold energy, $E_{min} \simeq 100$ GeV (Section 3.1). Cherenkov photon density on the ground increases linearly with energy (Section 2.2.4) which compensates zenith angle dependence. If energy of primary particle grows k–times with respect to E_{min}, then maximum zenith angle will follow relation

$$\phi_{z,max} = \arccos\left(\frac{\cos\phi'_z}{k^{\frac{1}{4}}}\right). \qquad (2.12)$$

[2)] Sensitivity is given as $\phi = 5\sqrt{\epsilon_B F_B \varepsilon \Omega}/\left(\epsilon_\gamma \sqrt{T A_{eff}}\right)$, where ϵ_B denotes background rejection efficiency, F_B is flux of background events, ϵ_γ stands for γ–ray detection efficiency, ε is given by efficiency of event selection (see Section 2.3.1), Ω is solid angle, T is observation time and A_{eff} is effective area. Factor 5 comes from the fact that minimum significance, needed for claim of successful detection, is 5σ. Taken from Nedbal [42].

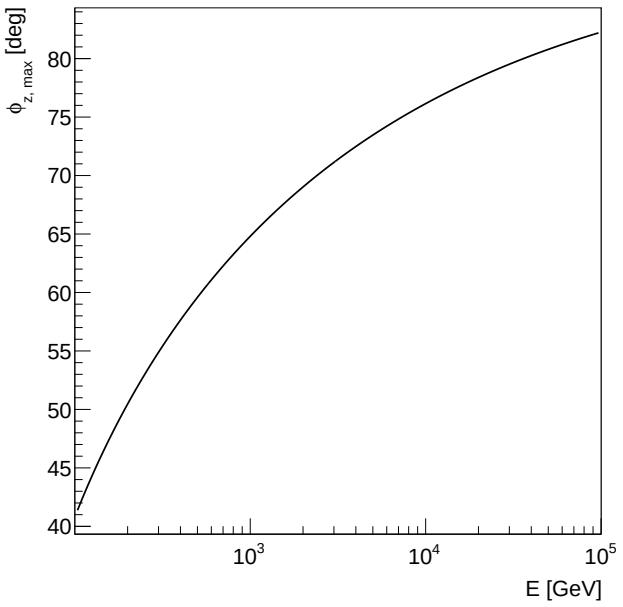

Figure 2.15: Maximum allowed zenith angle for observations at given energy according to Eq.(2.12).

This angle is illustrated in Fig.2.15 as a function of primary particle's energy.

It is important to mention that previous results are only rough estimates as the response of detector to Cherenkov light was not taken into account. Neither were these detectors simulated as imaging Cherenkov telescopes which are of primary interest to us. Therefore one has to regard results like e.g. Fig.2.15 only as estimates of basic air shower behaviour.

Advantage of large zenith angle observations lies in the increase of the collection area of an experiment. This can lead to improvement of sensitivity but performance of telescopes is also an important factor here. Larger areas of telescope dishes and better photon detection efficiency are desirable in future imaging atmospheric Cherenkov experiments in order to detect small amount of Cherenkov photons from showers at large zenith angles. It was found in Konopelko et al. [36] that sensitivities of telescope arrays are about the same for small and large zenith angles ($\sim 60^\circ$) assuming γ–ray spectral index $\geqslant 2.5$. Observations above 10 TeV have higher sensitivity when detecting γ–ray fluxes with the spectral index of $\geqslant 2.0$.

Disadvantage of large zenith angle observations is increasing ratio width/length of showers in telescope camera [36]. This means that γ–shower images at larger zenith angles have circular rather than elliptical shape and hence the reconstruction of their arrival directions is less accurate (see Section 2.3.1).

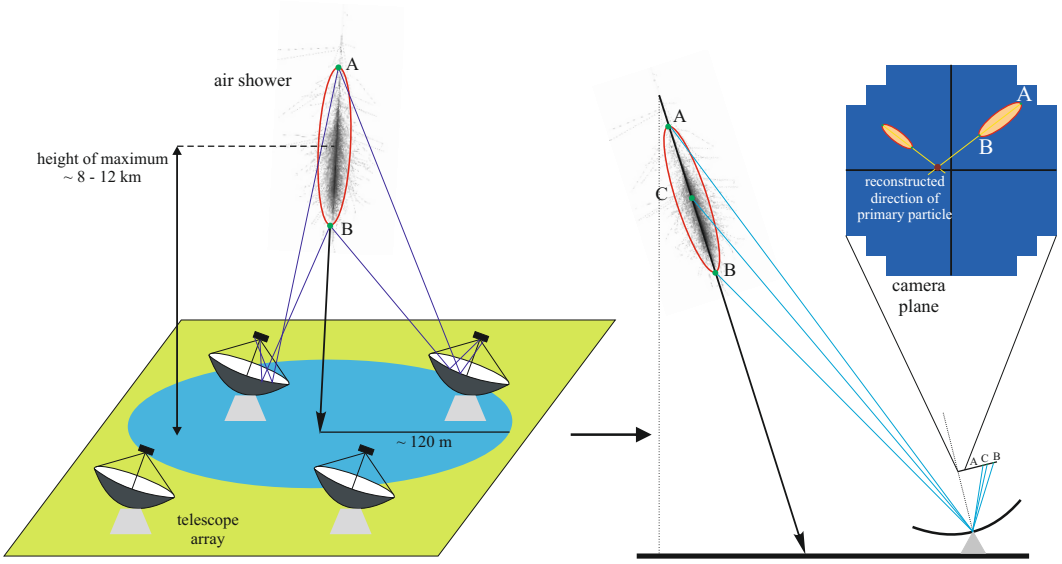

Figure 2.16: Sketch of imaging atmospheric Cherenkov technique. Left: Air shower caused by primary γ–ray is seen by telescopes which lie within the pool of Cherenkov photons generated in the shower. Right: Cherenkov photons are focused into telescope camera where image of air shower is produced. Taken from Štefánik [55].

2.3 Imaging atmospheric Cherenkov technique and signal processing

Imaging atmospheric Cherenkov technique (IACT) is a way for observation of γ–ray signal by detection of Cherenkov light from air showers using ground–based telescopes. A brief description of this method is given at the beginning of this Section. Parametrisation of acquired shower images and signal extraction along with application on real γ–ray source data are discussed in Sections 2.3.1 and 2.3.2, respectively. Method of testing for γ–ray signal presence (Section 2.3.2) is altered to allow testing for time variability of signal, see Section 2.3.3.

Principle of IACT is depicted in Fig.2.16. Cherenkov photons produced in air showers caused by cosmic rays are collected by individual mirrors of telescope into its focal plane. A camera consisting of photomultipliers is mounted in the focal plane of each telescope and impulses from impacting Cherenkov photons are converted into measurable signal. Every photomultiplier stands for one pixel in the resulting image, intensity of which is given in units of photoelectrons (p.e.). Primary selection of events is done by allowing into further analysis only those pixels that have intensity of at least 10 p.e. and at the same time are adjacent to the pixel with 5 p.e. or more. The opposite criterion is used simultaneously: a pixel is not counted in the shower image unless it has an intensity of at least 5 p.e. and its neighbouring pixel contains at least 10 p.e.

Showers can be detected either by single telescope (e.g. MAGIC experiment [3] before extension) or telescope array (see Fig.2.16), the latter being called stereoscopic method of detection which has several advantages. One of them is sig-

nificant reduction of background noise by adopting trigger condition regarding detection by multiple telescopes. At the same time it excludes the possibility of triggering the system by muons which hit single telescopes.

Another advantage concerns more precise reconstruction of primary γ–ray's arrival direction. This is achieved by superposition of elliptical shower images from several telescopes and subsequent interception of their major axes.

Very important is also larger area coverage due to higher number of telescopes. This results in instrumental ability to detect smaller γ–ray fluxes and hence the limit for detection is pushed to higher energies of primary radiation.

2.3.1 Image parameters

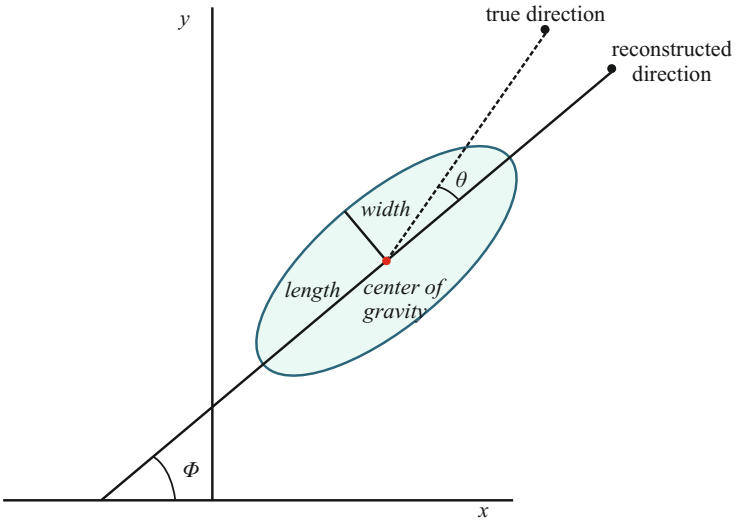

Figure 2.17: Hillas parameters describing air showers. *Length* and *width* stand for major and minor axis of elliptical image, respectively. *Center of gravity*, or shower image center, is given by $x_{\mathrm{CoG}} = \sum_{i=1}^{N} a_i x_i / \sum_{i=1}^{N} a_i$ where i is the index of one pixel contained in shower image with N pixels and a_i is intensity of given pixel. Analogously for y coordinate. Angular distance between reconstructed direction of an event and its true direction is denoted as θ. Another parameter, which is not shown in the picture, is the image amplitude A given as the number of photoelectrons contained in pixels within shower image. Taken from Štefánik [55].

Shower images have elliptical shape and are generally described by so called Hillas parameters [30]. For overview and explanation of these parameters see Fig.2.17, example of shower image as seen by the H.E.S.S.–type telescope is shown in Fig.2.18. Particularly important are the image amplitude, width and length. Selection cuts applied on these quantities greatly reduce background caused by cosmic ray nuclei. Summary of these cuts and their application on simulated and real data are given in the following.

Since shapes of showers induced by γ–rays and cosmic ray nuclei are very different (Section 2.2.2), background caused by the latter can be effectively rejected by applying proper selection cuts on length and width of shower image. Mean reduced scaled parameters were introduced [12] in order to describe images inde-

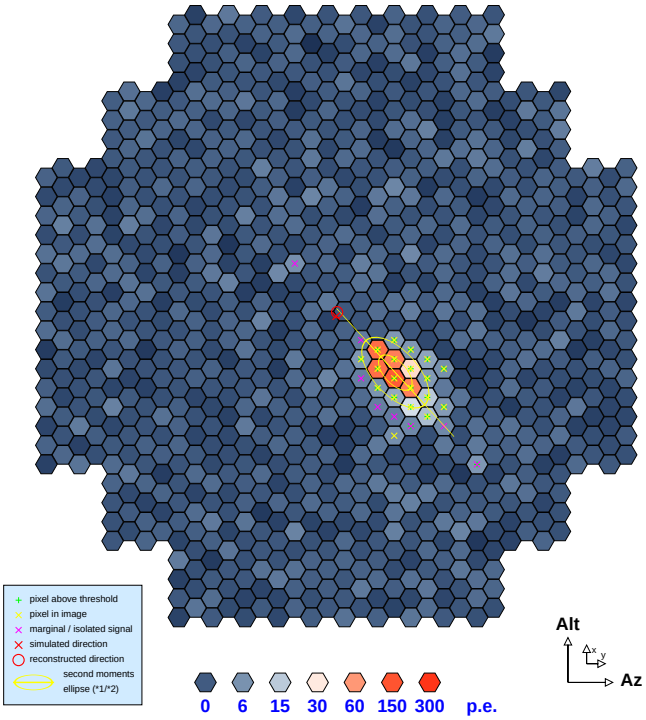

Figure 2.18: Shown is the parametrisation of shower image in the camera of H.E.S.S.–type telescope. Yellow crosses indicate pixels which are contained within the shower image, magenta crosses stand for marginal pixels not included in the image, red cross marks the simulated direction of primary γ–ray and red circle denoted reconstructed direction of shower. Yellow ellipse specifies the shower image, i.e. its width and length. This image was obtained by simulation of a shower induced by 1 TeV γ–ray and detected by four telescopes using `sim_telarray` program.

pendently of shower zenith angle, offset (see Section 2.3.2) and impact parameter, i.e. distance of shower impact point from telescopes. The mean reduced scaled width and length ($MRSW$ and $MRSL$) are defined as

$$MRSW = \frac{1}{N}\sum_{i=1}^{N}\frac{w_i - \langle w_i\rangle}{\sigma_i}, \quad MRSL = \frac{1}{N}\sum_{i=1}^{N}\frac{l_i - \langle l_i\rangle}{\sigma_i} \tag{2.13}$$

where w_i and l_i are width and length of shower image in the i–th telescope, N denotes the number of telescopes participating in detection. Mean values $\langle w_i\rangle$ and $\langle l_i\rangle$ are found in simulations and σ_i is corresponding standard deviation [42].

Example distributions of $MRSW$ and $MRSL$ are shown in Fig.2.19. Both simulated and real events (obtained by H.E.S.S.) were used for this purpose. γ–ray events comprise simulated showers induced by photons observed under the zenith angle of 20°. Real data originate from the γ–ray source Crab Nebula observed under the zenith angle of 50°. Distributions of hadronic events are illustrated by the means of simulated proton induced showers under zenith angle of 20° and so called off–source data which were taken from a part of sky with no

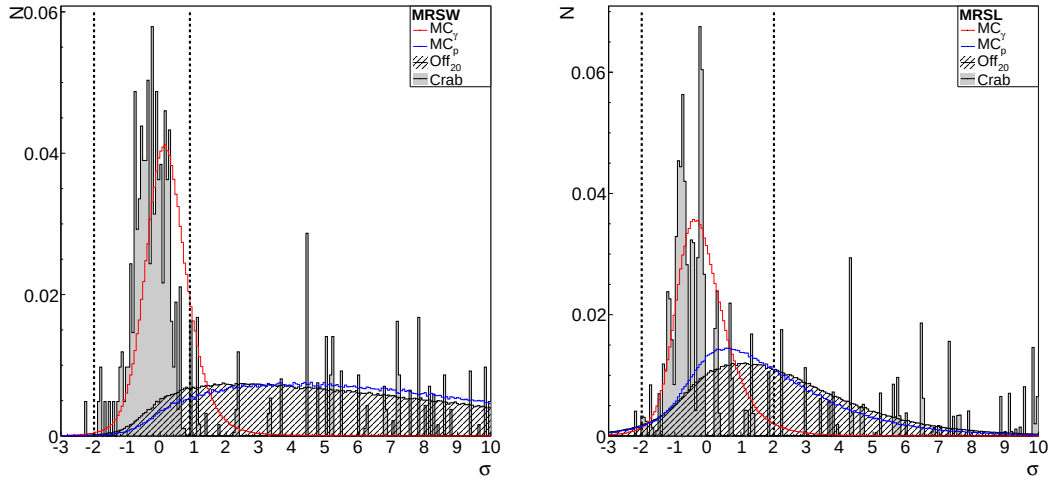

Figure 2.19: *MRSW* (left) and *MRSL* (right) distributions of simulated and real events. Red histogram stands for simulated events caused by γ–rays, blue one denotes simulated hadronic events. Histogram of real events from γ–ray source Crab Nebula was normalized to have the same area as distribution from simulated γ–ray events. Dashed lines represent values of standard cuts for scaled width and length, see Table 2.1. Taken from Štefánik [55].

γ–ray sources under the same zenith angle.

Images of showers initiated by nuclei are wider than those that are generated by γ–rays. Overall Cherenkov photon density on the ground is smaller in the case of the former due to more extensive lateral development of hadronic showers. This can be seen in Fig.2.19 where hadronic events have clearly wider distributions in scaled parameters. Therefore cuts regarding image width and amplitude have the best rejecting power.

Table 2.1 lists different sets of selection cuts for *MRSW*, *MRSL*, minimum of image amplitude A and maximum of θ^2 which denotes the square of angular distance from true position of the source. These cuts were implemented within the H.E.S.S. collaboration [12] and are optimised to achieve maximum background rejection. Apart from cuts on these quantities, selection criteria are aimed also at minimum number of telescopes participating in detection which is usually set to 2 telescopes.

Standard cuts are used for sources with Crab–like spectrum[3)], i.e. with spectral index $\Gamma \sim 2.6$. At the same time, γ–ray flux from these objects is around 10% of Crab flux. *Hard* cuts are optimised for sources with hard spectrum ($\Gamma \sim 2$) and γ–ray flux $\sim 1\%$ of Crab flux. *Loose* cuts are suited for sources which have flux comparable to that of Crab Nebula and softer spectral index $\Gamma \sim 3$. *Extended* cuts with broader interval of θ^2 are used for objects larger than common point–like sources, e.g. extended shells of SNRs. This is done in order to encompass as much γ–ray signal as possible and to fully describe complex morphology

[3)] Pulsar wind nebula Crab Nebula is the strongest non–variable γ–ray source in the sky. As such, it is regarded as a 'standard candle' in γ–ray astronomy and fluxes of various sources are given in units of Crab Nebula flux.

Table 2.1: Sets of selection cuts. Taken from Aharonian et al. [12].

Class of cuts	*MRSW*	*MRSL*	$A_{\min}$ [p.e.]	$\theta^2_{\max}$ [deg^2]
standard	(-2.0, 0.9)	(-2.0, 2.0)	80	0.0125
hard	(-2.0, 0.7)	(-2.0, 2.0)	200	0.01
loose	(-2.0, 1.2)	(-2.0, 2.0)	40	0.04
extended	(-2.0, 0.9)	(-2.0, 2.0)	80	0.16

of these sources.

2.3.2 Signal extraction

In data analysis it is necessary to determine whether potential excess of γ–ray events is related to some point source or happens entirely due to background fluctuation. Also the absolute strength of this excess needs to be calculated. Statistical method of Li&Ma [39] is commonly used for this purpose and is described in this section together with its application on real–source data.

Let N_{on} denote the number of events observed during time t_{on} from the region around suspected γ–ray source. The number of background events N_{B} has to be subtracted from this value in order to determine possible excess of signal in this area. These can be estimated from measurements off the presumed source, i.e. in region with no γ–ray sources. The amount of excess events from the source is then given by

$$N_{\mathrm{S}} = N_{\mathrm{on}} - N_{\mathrm{B}} = N_{\mathrm{on}} - \alpha N_{\mathrm{off}}, \tag{2.14}$$

where N_{off} denotes the number of events in the off–source region and α is normalization which relates areas of on– and off–regions. For example, this can be calculated as the ratio of observation times $\alpha = t_{\mathrm{on}}/t_{\mathrm{off}}$.

In order to determine statistical significance that the signal excess is not observed by chance, firstly an assumption of no γ–ray source in observed area has to be made. It means that both N_{off} and N_{on} counts are due to background only, i.e. $N_{\mathrm{S}} = 0$. This is the essence of the binomial test of the statistical significance S_{Bin}. In the case of large data samplea, significance is asymptotically given by [39]

$$S_{\mathrm{Bin}} = \frac{N_{\mathrm{S}}}{\sigma\left(N_{\mathrm{S}}\right)} = \frac{N_{\mathrm{on}} - \alpha N_{\mathrm{off}}}{\sqrt{\alpha\left(N_{\mathrm{on}} + N_{\mathrm{off}}\right)}}. \tag{2.15}$$

Here $\sigma\left(N_{\mathrm{S}}\right)$ is an estimate of the square root of the standard deviation of N_{S}. Alternative evaluation follows from asymptotically valid equation derived by Li & Ma $S_{LM} \approx \sqrt{-2\ln\lambda}$ where λ denotes maximum likelihood ratio [39], i.e.

$$S_{\mathrm{LM}} = \sqrt{2}\left\{N_{\mathrm{on}}\ln\left[\frac{1+\alpha}{\alpha}\frac{N_{\mathrm{on}}}{N_{\mathrm{on}}+N_{\mathrm{off}}}\right] + N_{\mathrm{off}}\ln\left[(1+\alpha)\frac{N_{\mathrm{off}}}{N_{\mathrm{on}}+N_{\mathrm{off}}}\right]\right\}^{\frac{1}{2}} \tag{2.16}$$

Estimation of background can proceed in accordance with various models. Two of these models are used predominantly, namely *Ring background region* and *Reflected background regions* [12]. First method relies on estimation of background from the ring region around source position, usually in the centre of field

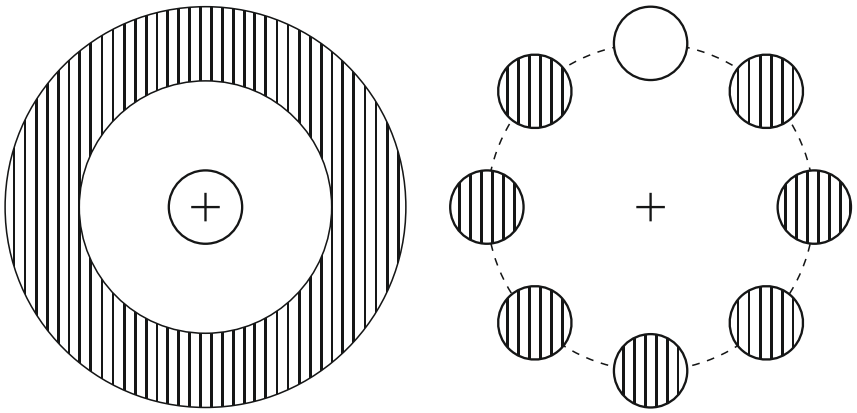

Figure 2.20: Left: *Ring region* method of background estimation. Right: *Reflected regions* method of background estimation. In both cases cross denotes the centre of the camera field of view. Areas filled with bars denote off–regions. White circle stands for the on region with source in its centre.

of view (see left panel of Fig.2.20). The on–region is a circle around this position with a radius given by a cut on θ^2. Inner radius of background ring is chosen such that overlapping of on– and off–regions is precluded. The overall area of the ring is usually chosen to match the condition for normalization factor $\alpha = 1/7$ [12], reason for that being reasonable distance from on–position and the edge of camera at the same time. Cameras of telescopes are not sensitive equally to incoming events. Therefore normalization coefficient needs to be scaled by acceptance[4)] of the camera.

Reflected background regions method determines background from multiple non–overlapping off–source regions with equal distances from the observation position. Distances are chosen to match offset of the true position of source from the centre of the camera field of view. Both on– and off–regions are circles with the same radius, see right panel of Fig.2.20. Normalization coefficient α is given by number of off–circles, $\alpha = 1/n$. No scaling by acceptance is needed because all regions are of the same size and are situated equidistantly from the camera centre.

Application of event selection and testing for source presence is here illustrated on PKS 2155–304 dataset. PKS 2155–304 is the active galaxy of BL–Lac type (see Section 3.3.2) which was extensively observed by H.E.S.S. telescopes [10]. Obtained data were at disposal in this work and comprise events observed at zenith angle of 20° for 0.44 hours of live time.

Fig.2.21 shows definitions of quantities used to describe events within the camera plane. Source was at the 0.5° offset from the centre of the camera field of view which means that the *reflected region* method of background estimation is particularly suitable in the following analysis. Since peaks in angular distribu-

[4)] Acceptance is sensitivity of camera to events passing selection cuts as a function of radial distance from the centre of its field of view [42]. Maximum sensitivity is assumed in this centre and acceptance is radially symmetrical. It can be determined from off–source data, since in this case only background events are detected and their number would be ideally constant, see e.g. [55].

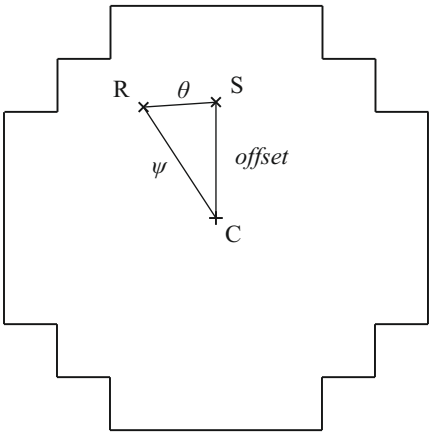

Figure 2.21: Quantities describing reconstructed position (R) of an event with respect to the camera centre (C) and source position (S).

Table 2.2: The number of on–source and off–source events, normalization coefficient α and significances of excesses from PKS 2155–304 calculated using Eqs.(2.15) and (2.16).

N_{on}	N_{off}	α	S_{Bin}	S_{LM}
144	15	1/7	29.8 σ	22.4 σ

tion θ^2 are indicators of γ–ray source in a given area, the primary objective was determination of this distribution.

Firstly an event selection was done according to standard set of cuts from Table 2.1. The region with on–events was determined as a circle around the true position of PKS 2155–304[5)] with the radius equal to the standard cut on θ^2. The number of off–regions was set to 7 and centres of these regions were at the same offset as the area with the source. The integrated amount of events from all regions is written in Table 2.2. The statistical test for non–zero signal was done according to Eqs.(2.15) and (2.16) and calculated significances of excesses are listed in Table 2.2. Statistical reliability over 22σ in both cases hints that PKS 2155–304 is indeed a source of VHE γ–radiation.

Precision of direction reconstruction is given by angular resolution of an instrument. This is investigated by the point spread function (PSF) in the case of the H.E.S.S. experiment. PSF is a sum of two Gaussian functions, first of them describing a peak in the centre of the on–region and the second one standing for a long tail of θ^2 distribution [19], [42]. It can be parametrised in the following way [12]:

$$\mathrm{PSF}\left(\theta^2\right) = A\left[\exp\left(-\frac{\theta^2}{2\sigma_1^2}\right) + A'\exp\left(-\frac{\theta^2}{2\sigma_2^2}\right)\right]. \qquad (2.17)$$

In Eq.(2.17), A is the amplitude and $\sigma_{1,2}^2$ are standard deviations of corresponding Gaussians. Angular resolution is defined as angular radius θ_{68} which restricts the area with 68% of all reconstructed events from a point source. This radius can

[5)] R.A.: 21 h 58 m 52.7 s, Dec.: $-30°\ 13'\ 18''$ [56]

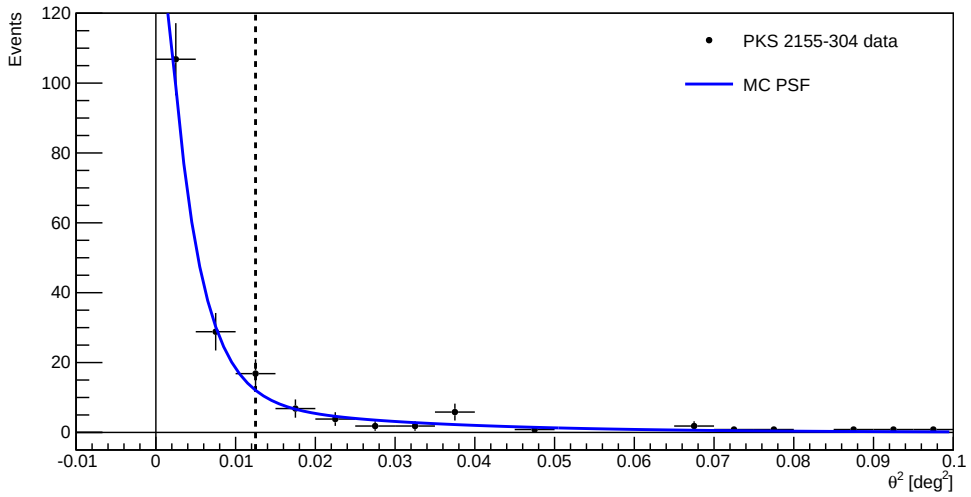

Figure 2.22: Angular distribution of event excess for PKS 2155–304 (black circles). Point spread function of the H.E.S.S. instrument (blue curve) obtained from a set of MC simulated γ–ray events with 20° zenith angle is plotted for comparison. It was normalised to the source excess distribution. Dashed line represents standard cut on θ^2.

be determined from the PSF fit to the angular distribution of simulated events from a point source as

$$\int_0^{\theta_{68}} \mathrm{PSF}\left(\theta^2\right) \mathrm{d}\theta = 0.68 \int_0^{\infty} \mathrm{PSF}\left(\theta^2\right) \mathrm{d}\theta. \tag{2.18}$$

Events passing selection cuts were put into bins of the same size as a function of the square of radial distance from PKS 2155–304 position. Resulting angular resolution after subtraction of background events is shown in Fig.2.22. PSF fit to Monte Carlo simulated data from a point source is also shown in this picture. Angular resolution of the H.E.S.S. instrument for given zenith angle is according to this fit and Eq.(2.18) given as $\theta_{68} = 0.1°$. It means that all objects of smaller radius are point–like for the H.E.S.S. set up. Correlation between θ^2 distribution of the real source and the PSF fit implies point–character of PKS 2155–304. It means that one has no indication that the VHE γ–radiation originates from an extended region.

2.3.3 Testing time variability of γ–ray flux

Variability of γ–ray flux over some period of time can help to restrict some key features of astrophysical sources, e.g. dimensions of emitting region (see Section 3.3). Therefore, it is important to determine whether a source is variable or not. It is a difficult task if the γ–ray flux in question is small or the variability timescale is short. Here, the method of Li&Ma [39] for γ–ray excess determination (Section 2.3.2) is modified in order to test sources for time variability of their flux. This method along with its application on the PKS 2155–304 data is described in this section.

The method of testing for presence of event excess relies on assumption of zero signal in the on–region, i.e. $\langle N_{\rm S}\rangle = 0$. Hence expectation value for event count in the on–region is given solely by background, $\langle N_{\rm on}\rangle = \langle N_{\rm B}\rangle$, and analogously expectation value in the off–region is $\langle N_{\rm off}\rangle = \langle N_{\rm B}\rangle/\alpha$ where α denotes normalization relating on– and off–regions. Therefore, the standard deviation of excess counts is found to be [39]

$$\begin{aligned}\sigma^2\left(N_{\rm S}\right) &= \sigma^2\left(N_{\rm on}\right) + \sigma^2\left(\alpha N_{\rm off}\right) = \\ &= \sigma^2\left(N_{\rm on}\right) + \alpha^2\sigma^2\left(N_{\rm off}\right) = \\ &= \langle N_{\rm on}\rangle + \alpha^2\langle N_{\rm off}\rangle \\ &= (1+\alpha)\langle N_{\rm B}\rangle \end{aligned} \tag{2.19}$$

Background expectation value $\langle N_{\rm B}\rangle$ in the on–region is evaluated from the whole dataset $N_{\rm on} + N_{\rm off}$ as

$$\langle N_{\rm B}\rangle = \frac{t_{\rm on}}{t_{\rm on}+t_{\rm off}}\left(N_{\rm on}+N_{\rm off}\right) = \frac{\alpha}{1+\alpha}\left(N_{\rm on}+N_{\rm off}\right), \tag{2.20}$$

where $\alpha = t_{\rm on}/t_{\rm off}$ was assumed. Assuming Eq.(2.14)and inserting Eq.(2.20) into Eq.(2.19), one arrives at Eq.(2.15) for the significance of γ–ray excess. One can see that

$$\begin{aligned}\langle N_{\rm on}\rangle &= \langle N_{\rm S}\rangle + \langle N_{\rm B}\rangle = \langle N_{\rm B}\rangle \\ \langle N_{\rm off}\rangle &= \langle N_{\rm B}\rangle/\alpha \end{aligned} \tag{2.21}$$

It follows from Eq.(2.21) that if one regards $\langle N_{\rm on}\rangle$ and $\langle N_{\rm off}\rangle$ as parameters in the Eq.(2.15), then the correspondence $\langle N_{\rm on}\rangle = \alpha\langle N_{\rm off}\rangle$ is valid.

The hypothesis of the zero signal is no more relevant when inspecting time variability of sources with already established excess of γ–ray events. Therefore, the null hypothesis is in this case given by the assumption that the signal has not changed from the reference value, e.g. the previous observation run in the dataset. One can assume that $\langle N_{\rm S}\rangle \neq 0$ such that the expectation value of event counts in the on–region is different from normalized quantity $\alpha\langle N_{\rm off}\rangle$ by some factor β:

$$\langle N_{\rm on}\rangle = \beta\alpha\langle N_{\rm off}\rangle, \quad \beta \neq 1. \tag{2.22}$$

Eq.(2.22) can be further rewritten with the use of $\langle N_{\rm on}\rangle = \langle N_{\rm S}\rangle + \langle N_{\rm B}\rangle$ as

$$\begin{aligned}\langle N_{\rm on}\rangle &= \beta\alpha\langle N_{\rm off}\rangle = \\ &= \beta\alpha\left(N_{\rm on}+N_{\rm off}-\langle N_{\rm S}\rangle-\langle N_{\rm B}\rangle\right) = \\ &= \beta\alpha\left(N_{\rm on}+N_{\rm off}-\langle N_{\rm on}\rangle\right) \\ \Rightarrow \langle N_{\rm on}\rangle &= \frac{\beta\alpha}{1+\beta\alpha}\left(N_{\rm on}+N_{\rm off}\right) \end{aligned} \tag{2.23}$$

The evaluation of $\langle N_{\rm B}\rangle$ can proceed as follows:

$$\begin{aligned}\langle N_{\rm B}\rangle &= \frac{\alpha}{1+\alpha}\left(N_{\rm on}-\langle N_{\rm S}\rangle+N_{\rm off}\right) \\ &= \frac{\alpha}{1+\alpha}\left[N_{\rm on}-\frac{\beta\alpha}{1+\beta\alpha}\left(N_{\rm on}+N_{\rm off}\right)+\langle N_{\rm B}\rangle+N_{\rm off}\right] \\ &= \frac{\alpha}{1+\alpha}\left[\frac{1}{1+\beta\alpha}\left(N_{\rm on}+N_{\rm off}\right)+\langle N_{\rm B}\rangle\right] \\ \Rightarrow \langle N_{\rm B}\rangle &= \frac{\alpha}{1+\beta\alpha}\left(N_{\rm on}+N_{\rm off}\right) \end{aligned} \tag{2.24}$$

Table 2.3: Listed is the number of the on– and off–events in the case of γ–ray source PKS 2155–304, normalization coefficient α, the number of excess events and their significance S_{LM} as measured by the H.E.S.S. telescopes. These values were taken from Aharonian et al. [10]. The rightmost two columns contain the average value of parameter β and the significance of time variability S_{var} calculated according to Eq.(2.27).

Period	N_{on}	N_{off}	α	N_{S}	S_{LM} $[\sigma]$	β	S_{var} $[\sigma]$
07/2002	637	234	1.063	388	13.0	1.75	5.03
10/2002	865	519	1.065	312	8.2	1.75	-1.99
11/2002	80	90	0.896	-0.65	-0.1	1.75	-3.73
06/2003	1396	4619	0.152	694	21.1	1.75	-4.23
07/2003	3169	13643	0.147	1164	22.1	1.75	-5.11
08/2003	3369	12955	0.147	1459	27.7	1.75	0.63
09/2003	185	697	0.148	82	6.7	1.75	0.31
09/2003	1005	3946	0.147	425	14.7	1.75	-0.25

The expectation value $\langle N_{\mathrm{S}} \rangle$ is using Eq.(2.24) determined as

$$\langle N_{\mathrm{S}} \rangle = \frac{\beta\alpha}{1+\beta\alpha}\left(N_{\mathrm{on}} + N_{\mathrm{off}}\right) + \langle N_{\mathrm{B}} \rangle = \frac{\alpha\beta - \alpha}{1+\beta\alpha}\left(N_{\mathrm{on}} + N_{\mathrm{off}}\right) \tag{2.25}$$

It follows from Eqs.(2.24) and (2.25) that

$$\begin{aligned} \langle N_{\mathrm{on}} \rangle &= \langle N_{\mathrm{S}} \rangle + \langle N_{\mathrm{B}} \rangle = \frac{\alpha\beta}{1+\beta\alpha}\left(N_{\mathrm{on}} + N_{\mathrm{off}}\right) \\ \langle N_{\mathrm{off}} \rangle &= \langle N_{\mathrm{B}} \rangle/\alpha = \frac{1}{1+\beta\alpha}\left(N_{\mathrm{on}} + N_{\mathrm{off}}\right). \end{aligned} \tag{2.26}$$

If expectation values in Eq.(2.26) are considered as parameters, then one finds out that $\langle N_{\mathrm{on}} \rangle = \alpha\beta\langle N_{\mathrm{off}} \rangle$. This result is the same as the one following from Eq.(2.21) apart from the additional factor β. Thus, Eq.(2.15) can be used for determination of source variability as well, provided that one exchanges coefficient α for $\alpha\beta$, i.e.

$$S_{\mathrm{var}} = \frac{N_{\mathrm{on}} - \beta\alpha N_{\mathrm{off}}}{\sqrt{\beta\alpha\left(N_{\mathrm{on}} + N_{\mathrm{off}}\right)}}. \tag{2.27}$$

The meaning of S_{var} is a statistical test whether the source flux has changed from the reference value. It has to be chosen in the very beginning and all the other numbers of signal events in the dataset are compared with this value. Derivation of relation analogous to (2.16) would proceed in a similar way and the final result can be again obtained by substitution $\alpha \to \beta\alpha$ [43].

The result given in Eq.(2.27) is completely independent of telescope multiplicity in particular observations, zenith angle of incoming events and total effective area of experiment in given layout. This is very useful in determination of γ–ray flux variability from sets of data with different observation conditions.

Application of Eq.(2.27) is demonstrated on the galaxy PKS 2155–304. Since the dataset used in Section 2.3.2 covers only short time scale (close to the shortest resolvable time variability by H.E.S.S., $\sim$ 0.5 h), more extensive set of results obtained in Aharonian et al. [10] is used here. Table 2.3 lists the number of the on– and off–events along with significances of event excesses in different periods between July 2002 and September 2003.

Parameter β is not a priori known and it has to be calculated from one chosen reference observation run using Eq.(2.22) with the assumption that $\langle N_{\rm on} \rangle = N_{\rm on}$. This was done separately for all periods in Table 2.3 and corresponding significances of signal variability against the given reference period were calculated. Table 2.3 contains only value of β averaged over all runs. Significances of time changes of source flux from an average signal were estimated according to Eq.(2.27). A positive or negative sign before each significance value corresponds to either excess or deficit of events in a given time period.

It is important to mention that only observations from June 2003 and afterwards were performed in the stereoscopic mode with two telescopes and only the last entry in Table 2.3 was obtained using three detectors. Observations in the single–telescope mode might have been less accurate with respect to the last three time periods in question which obviously give very similar results on time variability. Nevertheless, reliability over 5σ and 4σ in stereoscopic runs during July and June 2003, respectively, hint to the fact that PKS 2155–304 is source of time variable γ–ray emission. This is in agreement with results of the H.E.S.S. collaboration which reported variability on the scale of months, days and hours [10].

Method for analysing time variable fluxes presented in this work may be useful in determination whether flux from a particular source of γ–rays is changing with time or not. Further applications of this method are desirable, especially on raw data precisely divided in time periods under consideration in order to exactly determine possible variability time–scale.

3. Cherenkov Telescope Array

The advent and development of Cherenkov arrays in last decade made it possible to study very–high energetic cosmic ray sources in unprecedented detail and resulted in discovery and subsequent description of many new γ–ray sources. Particularly the H.E.S.S. project claims discovery of 90 TeV γ–ray objects from 2005 til the end of 2012 [56], almost two thirds of all detected TeV sources. Although this contributes very much to the progress of γ–astronomy, both area and energy coverage as well as size of current telescope arrays are not sufficient enough to undertake large sky surveys or determine cosmic ray acceleration scenarios and γ–ray origin in greater detail. Of great interest is also search for possible 'exotic' physics lying behind the dark matter or probing some aspects of fundamental physics, like Lorentz invariance violation. These science cases call for new generation of imaging atmospheric Cherenkov telescopes (IACTs) capable of pursuing the above goals.

Primary motivation of this Chapter is introduction to the planned Cherenkov Telescope Array (CTA), starting by description and comparison with current IACTs in Section 3.1. Considered configurations are presented in Sections 3.2. Finally, extragalactic object Centaurus A is discussed as possible target for CTA observations in Section 3.3.

3.1 CTA description

Short overview of Cherenkov Telescope Array and comparison with previous experiments is given here.

Current Cherenkov arrays comprise at most 5 telescopes and operate in energy range from roughly 50 GeV to 100 TeV. Properties of these IACTs are given in Table 3.1. Stereoscopic observations are of great importance in order to improve sensitivity and angular resolution. However, low energy regime is so far always covered only by one telescope, not to mention that observation time is reduced due to small number of telescopes in whole energy range. Therefore increased number of detectors should be primary advantage of new telescope array.

Cherenkov Telescope Array [1] is planned to cover broad energy band, i.e. 4 orders of magnitude, improving current limits on both sides of spectrum, from sub–100 GeV range up to several hundreds of TeV. This will be achieved using tens of telescopes of different sizes. Large number of telescopes will allow detailed studies of astrophysical objects with high sensitivity which is planned to upgrade current achievable values by a factor of $\sim$10 [8]. Apart from observations of single objects, simultaneous observations of multiple sources will be possible due to increased telescope number. Several groups of telescopes can be aimed at different positions with their fields of view overlapping. This way large sky surveys with less time consumption can be also done.

CTA is the first experiment to be run from two sites in both hemispheres. Northern site should focus on extragalactic sources. Because of this, it will work in the energy regime of $\sim$ 10 GeV $-$ 1 TeV and will not need as many small–sized telescopes intended for high–energy observations. Southern observatory with superior view on the Galactic plane will be aimed at observations of both

Table 3.1: Parameters of current IACTs. Shown are their geographic locations, altitude, number of telescopes and their area followed by number of pixels in telescope cameras and overall field of view. Last two columns contain values of threshold energy and sensitivity of given experiments. Taken from Hinton [31].

Instrument	Lat	Long	Alt	Telescopes		Pixels	FoV	Thres. Energy	Sensitivity
				#	Area				
	[°]	[°]	[m]		[m^2]		[°]	[GeV]	[% of Crab]
H.E.S.S.	-23	16	1800	4	107	960	5	100	0.7
H.E.S.S. II				1	614	2048	3.2		
VERITAS	32	-111	1275	4	106	499	3.5	70	0.7
MAGIC	29	18	2225	1	234	576	3.5	30	1.0
MAGIC II				1	234	1039			
CANGAROO–III	-31	137	160	3	57.3	427	4	400	15

galactic and extragalactic sources. It will operate in the wider energy range ~ 10 GeV $- 100$ TeV with larger field of view [8].

Demand for the whole sky coverage calls for construction sites around the latitude of $\sim 30°$. Great number of telescopes demands large flat areas (~ 10 km^2). Higher altitudes are also desirable in order to gain higher Cherenkov photon density. Deflection of charged particles in air showers due to the geomagnetic field causes enlargement of Cherenkov pool on the ground, i.e. decrease of photon density, and distortion of images. This makes the separation of γ–events from hadronic background less effective [54]. Therefore locations with lower values of the geomagnetic field component parallel to the surface are more appropriate. Some other requirements for CTA location sites include large number of clear–sky nights, low light pollution, good weather conditions, optimum infrastructure etc. All of these make only some locations suitable, map of which is shown in Fig.**??**.

3.2 Configurations

As CTA will operate over broad wavelength band, high concern about number and size of Cherenkov telescopes is in place. Telescopes of big dish areas are not needed for high energy observations and, vice versa, small telescopes are ineffective when detecting low energy showers. Therefore different telescope sizes are favourable and CTA operation range can be adequately divided into three energy intervals, following discussion in Actis et al. [8].

First of them, $\leqslant 100$ GeV regime, is characterized by large incoming γ–ray flux but small photoelectron yield from air showers. Moreover, sensitivity in this range is reduced because of worse γ–hadron separation, thus collection area as large as Cherenkov pool size is sufficient. In order to obtain good quality images, large telescopes situated in centre of array with diameter of approximately 20–30 m are needed. Observations with H.E.S.S. have shown that already two detectors greatly reduce hadronic–dominated background and improve sensitivity and angular resolution. This is even emphasized with higher number of telescopes. However, demanded dish size for CTA low energy regime makes the cost of telescopes higher, since price scales quadratically with diameter. Therefore,

Table 3.2: Possible arrangements of CTA South (A–K) and North (NA, NB) array giving number and field of view (in parenthesis) of large (24 m diameter), medium (12.3 m) and small (7.4 m) telescopes in cosideration. Taken from Bernlöhr et al. [21].

Layout	Large	Medium	Small
A	3 (5°)	41 (8°)	
B	5 (5°)	37 (8°)	
C		29 (8°)	26 (10°)
D		41 (7.4°)	16 (10°)
E	4 (4.6°)	23 (8°)	32 (10°)
F	6 (4.8°)	29 (6.3°)	
G	6 (5°)	9 (8°)	16 (10°)
H		25 (7°)	48 (10°)
I	3 (4.9°)	18 (8°)	56 (9°)
J	3 (4.9°)	30 (8°)	16 (9°)
K	5 (5°)		72 (9.5°)
NA	4 (5°)	17 (6°)	
NB	3 (5°)	17 (6°)	8 (8°)

either few very large telescope dishes or many smaller ones ($\sim 10-15$ m) should be used. Problem of proper triggering arises in the latter case, since none of telescopes receives enough light [8].

Middle energy range, from 100 GeV to several tens of TeV, is described by highest sensitivity of whole instrument in the range core around 1 TeV. Previous Cherenkov arrays have already shown that medium sized telescopes of ~ 12 m diameter with spacing roughly equal to Cherenkov pool radius (i.e. 130 m) are the best choice here. In the case of CTA, a grid of such telescopes placed around the large–sized ones will greatly enhance stereoscopic observations and collection area as well. This way shower impact point will always be situated next to multiple detectors resulting in lower trigger threshold.

High energy regime with energies reaching several hundreds of TeV is defined by bright images due to high photon density from showers, but on the other hand, incoming γ–ray flux is small. Hence an array of small sized ($\leqslant 3$ m diameter) or smaller number of larger ($\sim 3-5$ m) telescopes with wide field of view is desirable for these observations. First case scenario should use the standard 100–200 m spacing. The same applies for the second design but because of high photoelectron gain, spacing between some detectors can be increased to 300–500 metres. This way, much larger area is covered while still obtaining fine stereoscopic shower images. These telescopes will form outermost part of the whole array and they can be arranged in number of ways. Either they can be spaced equidistantly or form small subarrays with larger spacing. The latter solution offers also the possibility of detecting lower energy γ–rays provided the shower core is located inside the subcluster.

Monte Carlo simulation studies were done for a set of 275 telescopes [21] and subsequently different subarrays were analyzed. Table 3.2 lists considered

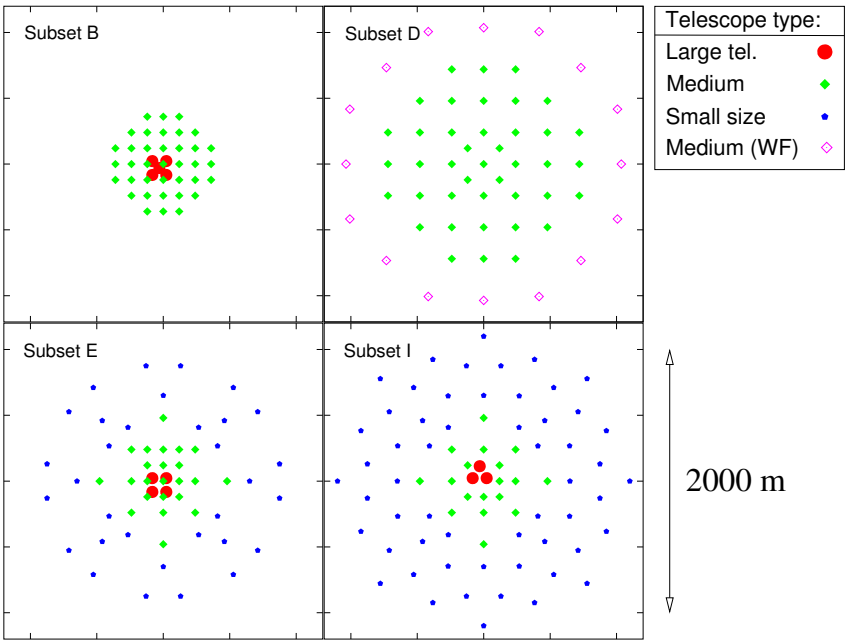

Figure 3.1: Candidate configurations for CTA. Top left stands for low–energy aimed subset B while top right panel illustrates subset without large sized telescopes for high energy observations. Bottom panels depict balanced layouts E and I, respectively. Taken from Bernlöhr et al. [21].

layouts of CTA for both locations. Arrays A, B, F, G are intended to obtain high overall sensitivity in low energy range whereas layouts C, D, H focus on high energy observations. Configurations E and I provide balance between both groups, achieving best sensitivity in the core range around 1 TeV. These are pictured in Fig.3.1 along with two other layouts focused on opposite sides of spectrum.

Choice of the final layout is given both by scientific requirements and overall cost. From purely scientific point of view the most appropriate subset can be picked by demanding certain value of sensitivity and angular resolution over the whole energy interval. It seems that the layout E fits best the goal curve which corresponds to improvement of sensitivity in current instruments by a factor of 10 [8]. Since configuration E is well balanced over whole CTA operation range and its price of 80 million € is reasonable and lower than in case of competing I design, it is, or at least one of its modifications, the most probable layout for CTA construction. It is compared to other γ–detection experiments in Fig.3.2. Its sensitivity as well as angular resolution is improved by a factor of ten for ten–image analysis, resulting in high–energy resolution of ~ 1 arcminute.

3.3 Centaurus A as a possible CTA target

Centaurus A (NGC 5128, Cen A) is the nearest active radio galaxy of Fanaroff–Riley I type, distance from Earth being 3.4 Mpc [33]. In the centre of the galaxy is situated very compact black hole with diameter $\leqslant 1$ pc and mass of approximately

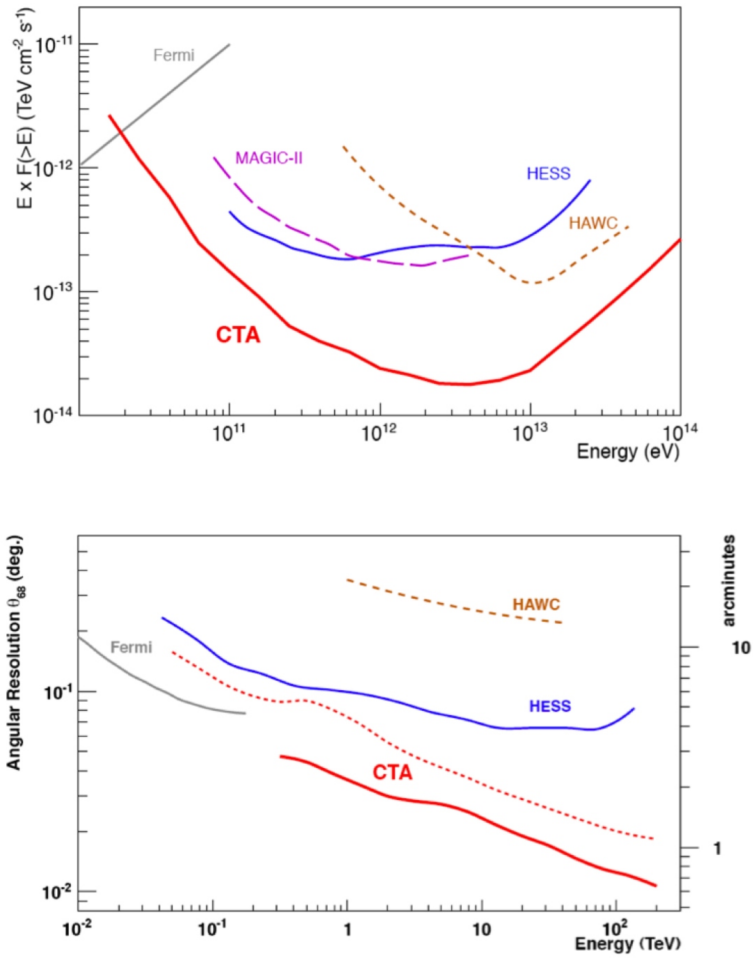

Figure 3.2: Comparison of CTA performance with some current and future experiments. Top: sensitivity of instruments. Bottom: angular resolution of instruments. Taken from Martinez [7].

$5.5 \times 10^7\ M_\odot$[1)] [22]. Emission from the active galactic nucleus (AGN) happens via jets which become non–relativistic and expand into plumes after roughly 5 kpc. Both nucleus and jets are visible in radio and X–ray wavelengths. The galaxy possesses two radio lobes extending to distance of 250 kpc from the nucleus and a gaseous torus orthogonal to jets with the nucleus at its centre [33]. Cen A is considered a non–blazar galaxy, meaning the jets do not point directly towards Earth but are rather inclined in range of $15° - 80°$ [32].

Pierre Auger Collaboration (PAO) reported an anisotropy of observed ultra–high energy cosmic ray (UHECR) events at 99% confidence level [5, 6]. Cosmic ray nuclei with energies above 57 EeV were found to correlate with some of nearby AGN ($\leqslant$ 75 Mpc from Earth) within circles of 3.1° radius. After 15/4 years of PAO observations between 2004 and 2007 two such events were detected from the Cen A neighbourhood.

Observations of electromagnetic spectrum from radio to VHE γ–rays provide

[1)] One solar mass: $1M_\odot = 2 \times 10^{30}$ kg

indirect information about possible processes in the vicinity of Cen A producing ultra–high energy species. Therefore, next sections are aimed at recent results on this topic and discussion of CTA role in this field.

3.3.1 Previous γ–ray observations

H.E.S.S. observations

VHE region of Cen A energy spectrum was observed by H.E.S.S. [13] between 2004 and 2008, totalling 115 hours of live time. Observations were done under offset $0.5^\circ - 0.7^\circ$ from core position of radio emission, allowing reflected background analysis. γ–ray signal above energy 250 GeV was detected with significance of 5σ. The fit to the point spread function revealed point character of source correlated with radio core and inner jet. Differential energy spectrum was determined as [13]

$$\frac{\mathrm{d}N}{\mathrm{d}E} = (2.45 \pm 0.52_{\mathrm{stat}} \pm 0.49_{\mathrm{sys}}) \times 10^{-13} \left(\frac{E}{1\ \mathrm{TeV}}\right)^{-\Gamma}\ \mathrm{cm}^{-2}\ \mathrm{s}^{-1}\ \mathrm{TeV}^{-1} \quad (3.1)$$

with power law index being $\Gamma = 2.73 \pm 0.45_{\mathrm{stat}} \pm 0.2_{\mathrm{sys}}$. Integral spectrum above threshold is equal to $F_\gamma(E > 250\ \mathrm{GeV}) = (1.56 \pm 0.67_{\mathrm{stat}}) \times 10^{-12}\ \mathrm{cm}^{-2}\ \mathrm{s}^{-1}$ [13]. This value amounts to 0.8% of Crab Nebula flux and to apparent luminosity of $L(E > 250\ \mathrm{GeV}) = 2.6 \times 10^{39}\ \mathrm{erg\ s}^{-1}$[2)]. Finally, no significant variability of γ–ray flux was discovered over periods ranging from half hour to months.

Fermi–LAT observations

Fig.3.3 shows γ–ray energy spectrum of Cen A above 100 MeV as measured by satellite Fermi–LAT [4] along with H.E.S.S. data points. Recently, it has been found out that simple power law with calculated index $\Gamma \approx 2.7$ does not fit the Fermi spectrum very well unless spectral break is introduced into the model [50]. This 'broken' power law results in two different normalizations and indexes, the break energy being equal to $E_{\mathrm{b}} = (4.00 \pm 0.09)$ GeV [50]. Dividing the whole data set into two regions given by this value and modeling two energy regions separately, the spectral indices and fluxes are given as [50]:

$$\begin{aligned} 0.1 - 4\ \mathrm{GeV}: &\quad \Gamma = 2.74 \pm 0.02,\ F_\gamma = (1.68 \pm 0.04) \times 10^{-7}\ \mathrm{cm}^{-2}\mathrm{s}^{-1} \\ 4 - 100\ \mathrm{GeV}: &\quad \Gamma = 2.09 \pm 0.2,\ F_\gamma = (4.20 \pm 0.64) \times 10^{-10}\ \mathrm{cm}^{-2}\mathrm{s}^{-1} \end{aligned} \quad (3.2)$$

Both of these power law functions are shown in Fig.3.3. Extrapolation of power law from the energy region of $(0.1 - 4)$ GeV to the highest energies does not match neither HE Fermi data above 4 GeV nor H.E.S.S. spectrum above 250 GeV, which is greatly underestimated in this case. On the other hand, power law with index 2.09 shows some degree of correlation with VHE data. Energy spectrum above the break energy of 4 GeV flattens rather then falls steeper what is expected to be a sign of at least one additional component in γ–ray emission [50].

No flux variability on time scales of 15, 30, 45 and 60 days was found [50]. This, along with no variability observed by H.E.S.S. [13], makes determination

[2)] 1 erg = 10^{-7} J = 6.2×10^{11} eV

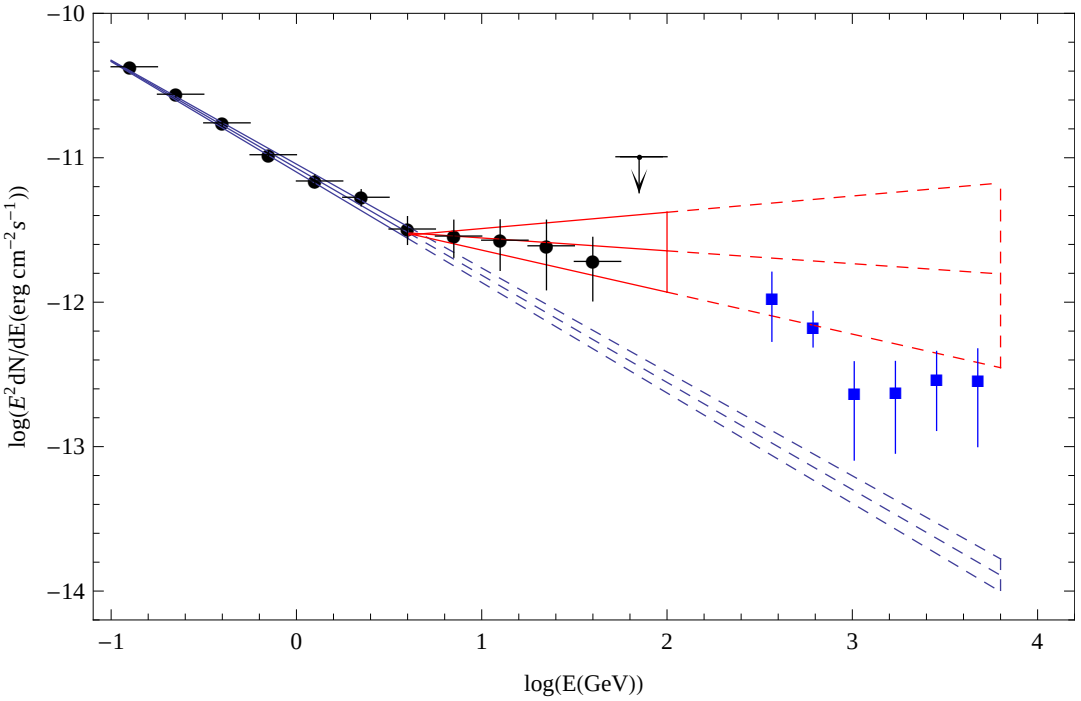

Figure 3.3: γ–ray spectrum as measured by Fermi–LAT (black circles) and H.E.S.S. (blue squares). Blue lines denote a power–law with spectral index 2.74, red lines represent power law with index 2.09. Dashed lines are extrapolations of these power laws to highest energies. Taken from Sahakyan et al. [50].

of emission region more difficult. An upper limit for the size of this region $R \leqslant Dct_{\mathrm{var}}/(1+z)$ could be calculated for variability time scale t_{var} [38]. Here z is the redshift and $D = \gamma\,(1 - \beta\cos\theta)^{-1}$ is Doppler factor where θ denotes the viewing angle and β is the speed of emitting region. It is worth to note that time resolving capabilities of current instruments are not sufficient enough to detect variability of weak signal like that from Cen A.

3.3.2 Spectral energy distribution

Spectral energy distribution (SED) of Cen A was measured from radio to HE γ–ray wavelengths by various satellite experiments. Fig.3.4 shows two peaks in SED around 4×10^{-2} eV and 170 keV. Overview of possible leptonic–origin scenarios for radiation production explaining SED shape and spectrum observed by Fermi and H.E.S.S. is given in this section.

The whole energy spectrum up to GeV energies with both peaks is successfuly described by synchrotron self–Compton (SSC) model which can be extended from blazars with jets inclined to the line of sight to other non–aligned AGN [4, 38, 48]. Its essential feature is leptonic origin of electromagnetic radiation. Relativistic electrons contained within plasma blobs inside the jets are exposed to a magnetic field of rotating black hole. As a consequence, electrons emit synchrotron photons with energies around the first peak in SED. This first generation of synchrotron photons serves as a target for the very same population of parent electrons which are inversely Compton–scattered, resulting in second peak in distribution. As

can be seen in Fig.3.4, SSC model [4] fits well the data from radio to X–ray wavelengths but fails to incorporate H.E.S.S. measured spectrum. Discrepancy is also found between the SSC model and Fermi data [50].

To explain VHE sector of SED, several different models have been proposed. An extended SSC model with multiple plasma blobs in jets considered to be the place of synchrotron radiation is studied in Lenain et al. [38]. Two main scenarios can be assumed here. Either the line of sight is coincident with the velocity vector of one blob or it can point in the gap between three blobs. In both cases, blobs moving near the line of sight receive Doppler boost needed for TeV emission, the biggest contribution coming from blobs moving at zero viewing angle. This model was first applied to the active radio galaxy M 87. It describes well TeV spectra from several other misaligned AGN. Hence it attempts to unify the theory of γ–ray emission in blazars[3)] with other radio galaxies. However, when applied to Cen A, it was found that the model does not match H.E.S.S. data presuming the second SED peak existence due to inverse Compton scattering, as is usual. On the other hand, assuming the peak is of synchrotron origin, VHE spectrum is nicely explained but only for the sake of not including the radio–UV data. Multi–blob model introduces some degree of time variability due to both variable blob size and rotations of jets resulting in different viewing angles and thus different Doppler factors. Lack of any significant variability in Fermi and H.E.S.S. observations of Cen A seems to contradict this model as long as new observations with superior time resolution reveal some sort of time variability.

Another way of TeV–gamma production evolves from $\gamma\gamma$–absorption process. γ–rays of TeV energies emitted near the galaxy nucleus interact with starlight in the interstellar medium of the host galaxy [53] with probability $\sim 1\%$. Produced e^-e^+ pairs then undergo synchrotron radiation and/or inverse Compton scattering which results in VHE gamma radiation from an extended region. Since particle pairs are isotropized, final TeV γ–rays should produce small halo, approximately 4 arcmin in diameter. The fine structure of halo cannot be distinguished at present time because resolving capabilities of H.E.S.S. amount only roughly to 5 arcmin. However, in Sahakyan et al. [50] it is argued that overall efficiency of the process is low and a large flux of primary gamma rays would be needed.

3.3.3 Hadronic origin of VHE gamma rays

Apart from leptonic models of TeV emission from Cen A there are also possible explanations of this radiation relying upon its hadronic origin. Two such most probable scenarios of VHE γ–ray production are described in this section, namely interactions of protons with γ–rays and photodisintegration of iron nuclei. Moreover, these models attempt to estimate expected number of UHECR events as should be measured by PAO.

[3)] According to unification theory of active galaxies [47], blazars (BL–Lac objects) are effectively sub–class of wider group of radio galaxies with an active nucleus. Jets are pointed towards observer (Earth) in the case of blazars unlike other radio galaxies. This way, particle blobs always move in the line of jet emission and straight to the observer. As a consequence, emitted γ–rays are Doppler boosted and TeV radiation is observed. Blazars were the only detected TeV emitters before H.E.S.S. observations of non–aligned active galactic nuclei M 87 [11] and Cen A. Blob–in–jet model is successful in explaining VHE radiation from blazars and it is therefore reasonable to extend this model to other radio galaxies as well.

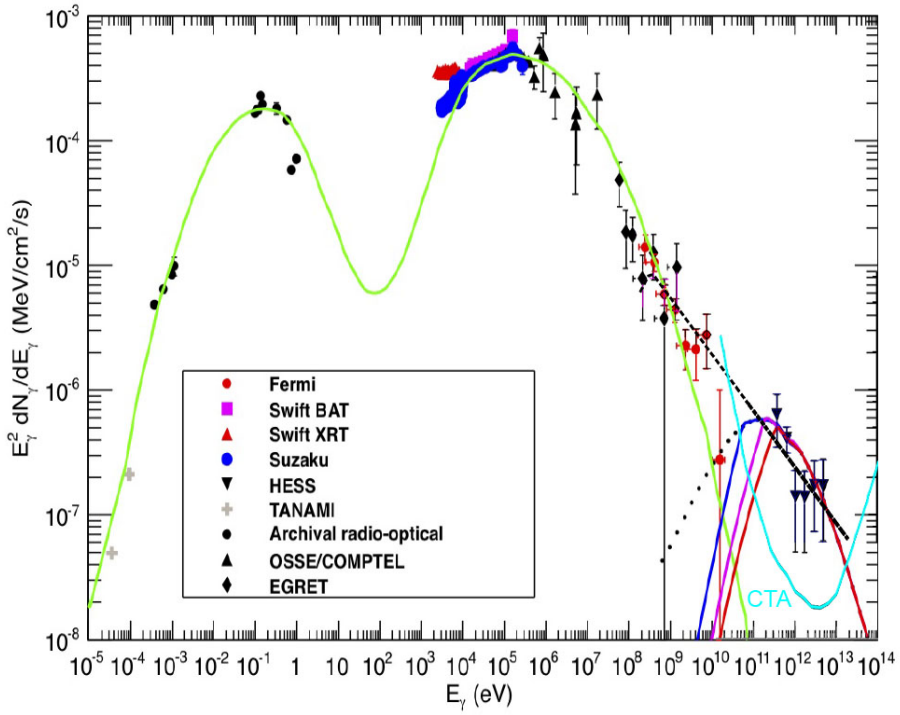

Figure 3.4: Spectral energy distribution of γ–ray emission from Cen A core region. Green curve represents SSC–fit performed in Abdo et al. [4]. Blue, magenta and red curves denote hadronic components of γ–ray emission produced in $p\gamma$ interactions with spectral break energy of protons equal to 4, 13 and 25 TeV, respectively, taken from Sahu et al. [51]. Black dashed line is prediction for hadronic component of γ–ray emission due to photodisintegration of iron nuclei taken from Joshi et al. [34]. Cyan curve stands for expected sensitivity of design E of Cherenkov Telescope Array taken from Acharya et al. [7].

Proton–gamma interactions

Protons (or heavier nuclei in more general case) can reach ultra–high energies by the means of Fermi acceleration. Their energy spectra are given by power law $\mathrm{d}N/\mathrm{d}E \propto E^{-\alpha}$, where a constant $\alpha \geqslant 2$. These protons then interact with photons coming from inverse Compton scattering around second SED peak [51] and produce Δ–resonance which decays via two channels:

$$p + \gamma \rightarrow \Delta^{+} \rightarrow \begin{cases} p + \pi^{0} \rightarrow p + 2\gamma, & 2/3 \\ p + \pi^{+} \rightarrow n + e^{+} + \nu_{e} + \nu_{\mu} + \bar{\nu}_{\mu}, & 1/3 \end{cases} \tag{3.3}$$

Relevant option is the first one with VHE γ–production probability of 2/3. Cross–section for $p\gamma$ interaction via Δ–resonance is $\sigma_{\Delta} \sim 0.5$ mb[4)].

It follows from kinematics [51] that protons and target photons have to satisfy a matching condition in order to produce Δ–resonance:

$$E_{p}\epsilon_{\gamma} \simeq 0.32\ \Gamma D, \tag{3.4}$$

[4)] Given value is according to Sahu et al. [51] where it is used without any reference. Somewhat smaller value of ~ 0.3 mb seems to be justifiable by data from Particle Data Group [45]

where E_p and ϵ_γ are respectively proton and target photon energy as measured by Earth observer, Γ is Lorentz factor of the jet and D denotes its Doppler factor[5]. This equation can be further modified into condition for energies of target γ–rays and final photons from π^0–decay assigned as E_γ [51]:

$$E_\gamma \epsilon_\gamma \simeq 0.032\ D^2. \tag{3.5}$$

Model of $p\gamma$ interactions [51] relies on values of parameters taken from SSC model [4], in particular $D = 1$ and $\Gamma = 7$. Putting these values along with photon energy of second SSC peak $\epsilon_\gamma^{\rm peak} \simeq 170$ keV into Eqs.(3.4) and (3.5) one gets:

$$\begin{aligned} E_p^{\rm peak} &\sim 13\ {\rm TeV} \\ E_\gamma^{\rm peak} &\sim 190\ {\rm GeV} \end{aligned} \tag{3.6}$$

where $E_\gamma^{\rm peak}$ is an approximate value of the final photon peak energy and $E_p^{\rm peak}$ is the primary proton energy.

The photon flux at energy $E_\gamma^{\rm peak}$ was found as a fit to H.E.S.S. data [51]. Then, the model energy spectrum of hadronic component was calculated. Fixed proton spectral index was $\alpha = 3.08$, coresponding to H.E.S.S.–measured value. Results can be seen in Fig.3.4 along with leptonic SSC model. Some difficulties might arise because of high proton luminosity at the peak energy $E_p^{\rm peak}$. Adopting the distance of Cen A, $d \sim 3.5$ Mpc, and particle blob size, $R_b = 3 \times 10^{15}$ cm, proton luminosity amounts to $L_p\left(E_p^{\rm peak}\right) = 4 \times 10^{45}$ erg s^{-1}. This value is close to that of Eddington luminosity[6] $L_{\rm Edd} \sim 1.3 \times 10^{46}$ erg s^{-1} $(M/10^8 M_\odot)$ [47]. The model of $p\gamma$ interactions can be successful only if this limit value is not exceeded. Thus a proton spectral break is introduced [51] at the energy $E_p^{\rm break}$. Proton power law spectrum hardens (flattens) below this value with spectral index fixed as $\alpha = 2$ and the resulting γ–ray flux is smaller. Fig.3.4 shows calculated spectra of VHE γ–rays for different values of the proton break energy.

The flux of ultra–high energy protons above 57 EeV was calculated using the same model [51] as $F(> 57\ {\rm EeV}) = 1.6 \times 10^{-13}$ erg cm^{-2} s^{-1}. The number of expected events detected by PAO in 15/4 years was estimated to be $N_{\rm UHE} = 3.7\,\zeta$. Probability ζ of protons escaping from the source was roughly 50% and therefore $N_{\rm UHE} \sim 1.9$.

The spectral break in hadronic component of VHE γ–rays is characteristic feature of $p\gamma$–model. It describes well H.E.S.S. data points and reconstructs the number of observed ultra–high energy events from the direction of Cen A. However, it clearly underestimates the HE data as measured by Fermi and does not account for the needed second component in this energy range. Another problem is related to the estimation of proton escaping probability, $\zeta = 0.5$, which is not supported by any argument. Finally, it is argued in Sahakyan et al. [50] that the source luminosity of proton–injection is larger than the usual average jet power $\sim 10^{43} - 10^{44}$ erg s^{-1}.

[5] $D = \Gamma^{-1}\,(1 - \beta\cos\theta_{\rm obs})^{-1}$, β being speed of the jet and $\theta_{\rm obs}$ is the jet viewing angle.

[6] Eddington luminosity is the maximum radiative power that an accretion–powered source can maintain [47]. In other words, continuous radiation outwards compensates the gravitational force, i.e. the source remains in equilibrium. When the Eddington luminosity is exceeded, the source initiates rapid outflow of material which is not the case of Cen A.

The model of proton interactions with γ–rays should therefore be regarded only as one potential model for TeV–gamma production and not the final solution to observed data from wider energy range starting at several tens of GeV.

Photodisintegration of iron nuclei

Apart from protons, heavier nuclei can also be emitted in the core region of Cen A. Corresponding models of TeV emission are then based on photodisintegration of these nuclei by photons of leptonic origin around second SED peak. In one particular case production of only iron nuclei can be assumed [34].

According to Joshi et al. [34], photons from inverse Compton scattering around the peak energy $\epsilon_\gamma^{\mathrm{peak}} \sim 170$ keV interact with iron nuclei with energy $E_{Fe}^{\mathrm{peak}} = 2.8$ TeV. Photodisintegration leads to production of nucleons and daughter nuclei which subsequently emit VHE γ–rays through de–excitation. Energy of these γ–rays can be estimated as

$$E_\gamma = \frac{2\bar{E}_{\gamma,Fe}E_N}{m_N}, \tag{3.7}$$

where $\bar{E}_{\gamma,Fe} \sim 2-4$ MeV is the average energy of a photon emitted by Fe nucleus in its rest frame [34], E_N and m_N are energy and mass of a single nucleon. Energy of γ–ray flux peak is found by taking $E_N^{\mathrm{peak}} = E_{Fe}^{\mathrm{peak}}/56 = 50$ GeV, $\bar{E}_{\gamma,Fe} = 4$ MeV and inserting it in Eq.(3.7):

$$E_\gamma^{\mathrm{peak}} \sim 400 \text{ MeV}. \tag{3.8}$$

Hadronic component of high–energy photon spectrum calculated for the case of iron nuclei photodisintegration is shown in Fig.3.4 [34].

The expected number of UHECR events detected by PAO obtained within this model is $N_{\mathrm{UHE}} = 2$. Luminosity of iron nuclei with energy above 55 EeV was found to be $\sim 10^{42}$ erg s^{-1} [34]. However, the luminosity of these nuclei around the peak energy was in the same work estimated as $\sim 10^{46}$ erg s^{-1}, i.e. of the same order of magnitude as the Eddington luminosity. One must also account for unusually high injection power in the core of Cen A.

Assumed photon spectral index in the model was $\Gamma = 2.45$ which agrees with index measured by H.E.S.S. within its error range (Section 3.3.1). It is somewhat larger than the index calculated for the second component in high energy spectrum in Fermi data [50] but mentioned results included only statistical errors and did not comprise systematics. Thus, it is reasonable to regard photodisintegration of Fe nuclei by low–energy photons as a possible explanation of Cen A γ–ray spectrum from ~ 4 GeV up to TeV energies.

3.3.4 CTA contribution

There are several reasons for future observations of γ–rays from Cen A by Cherenkov Telescope array. Some of them are highlighted below.

Gamma–emission from Cen A above 250 GeV cannot be explained by conventional models used for other active galactic nuclei. At present time, the knowledge of the origin of VHE γ–rays in astrophysical objects regarding its leptonic or hadronic character is poor. This is the case not only of active radio galaxies but other sources, e.g. supernova remnants, as well. Therefore narrowing

the wide range of models potentially describing high–energy γ–radiation in the case of Cen A could be helpful in establishing a more general concept of γ–ray production.

To date, no astrophysical object was recognized as a source of cosmic rays with energies above several EeV. Since observed γ–rays are only secondary products of interactions in sources, it is not possible to definitely prove the presence of UHECR in a given object in this way. However, models building on interactions of hadrons with low–energy photons in the jets of Cen A can put some constraints on the possibility of ultra–high energy cosmic ray production.

In order to resolve these issues, better telescope array performance, offered by CTA, is needed. Fig.3.4 shows the curve of CTA differential sensitivity along with two models of γ–ray hadronic component. CTA should be able to distinguish these two scenarios above $\sim$ 20 GeV or measure the composite contribution of both.

It is possible that final γ–ray energy spectrum is due to several components, in most general case both hadronic and leptonic. If this is the case, localizing the emission region more precisely would help to confirm or dismiss some models. CTA angular resolution of $\sim 1'$ will improve previous observations by a factor of 5. Thus, CTA will be able to determine whether TeV emission originates in compact region around the active nucleus and nearby inner jets of Cen A or it comes from its extended regions, possibly interfering with its giant radio lobes.

Another means of finding upper limits on emission region is by measuring time variability of the γ–ray signal. No variability of Cen A was found in Fermi and H.E.S.S. datasets which is unusual for active galaxies [47]. This can be thought as a result of very faint signal from Cen A or shorter variability time scales than currently resolvable. CTA with time resolution less than one minute and better sensitivity in a wider energy range should be able to detect variations in γ–ray flux on sub–minute time scales, if present.

Because of the above mentioned reasons, Cen A should be considered as a promising object to be pursued by CTA in the near future. In particular, measurements in both low– and middle– energy regimes with the higher number of telescopes are needed in order to fill the observational gap between $\sim 20 - 250$ GeV. Such experiments are believed to resolve TeV γ–ray signals with higher precision and to draw conclusions on particle production mechanism in this nearest AGN.

Conclusions

The aim of this thesis was the study of possible production and acceleration processes of cosmic rays in astrophysical objects. I have put special emphasis on simulations and detection techniques of very high energetic γ–rays, since they carry indirect information on parent cosmic rays.

Imaging atmospheric Cherenkov telescope arrays (IACTs) were described as the successful ground based experiments aimed at γ–astronomy. Cherenkov Telescope Array (CTA), a next generation of IACTs in preparatory phase, was presented. Scientific outcome from this experiment is expected to be priceless and active involvement in this project is in progress.

I determined the confidence level of signal from extragalactic source PKS 2155-304 in order to demonstrate analysis methods of real data obtained by IACTs, in particular by the H.E.S.S. collaboration. Fit of the point spread function (PSF) to the simulated events from γ–ray point source was compared with the angular distribution of PKS 2155-304. Agreement was found between this distribution and PSF from which follows that given source is point–like in nature.

The observations of cosmic γ–rays are effectively done by the detection of Cherenkov light produced during the evolution of air showers. Therefore, I performed simulations of air showers induced by charged particles and γ–rays in order to gather basic information about air shower development. Along with that, I simulated distributions of Cherenkov light produced from air showers for various initial conditions.

Statistical test for time variability of γ–ray sources was presented. I applied this test on long–term data from PKS 2155-304 and obtained the result of significant γ–ray flux variability on monthly scale.

The nearest active galaxy Centaurus A was put forward as an interesting target for CTA telescopes. Different production processes of VHE γ–radiation in this source were studied in detail, particularly photomeson production and photodisintegration of iron nuclei. Conclusive proof of either of studied mechanisms is still missing and the improved performance of CTA instrument will be needed for this purpose.

Bibliography

[1] CTA official website. http://www.mpi-hd.mpg.de/hfm/HESS/. 20. 3. 2013.

[2] KASCADE. http://www-ik.fzk.de/KASCADE_home.html/. 1. 3. 2013.

[3] MAGIC official website. http://magic.mppmu.mpg.de/. 27. 3. 2013.

[4] Abdo, A. A., et al. Fermi Large Area Telescope View of the Core of the Radio Galaxy Centaurus A. *Astrophys. J.719* (Aug. 2010), 1433–1444.

[5] Abraham, J., et al. Correlation of the Highest-Energy Cosmic Rays with Nearby Extragalactic Objects. *Science 318* (Nov. 2007), 938–.

[6] Abraham, J., et al. Correlation of the highest-energy cosmic rays with the positions of nearby active galactic nuclei. *Astroparticle Physics 29* (Apr. 2008), 188–204.

[7] Acharya, B. S., et al. Introducing the CTA concept. *Astroparticle Physics 43* (Mar. 2013), 3–18.

[8] Actis, M., et al. Design concepts for the Cherenkov Telescope Array CTA: an advanced facility for ground-based high-energy gamma-ray astronomy. *Experimental Astronomy 32* (Dec. 2011), 193–316.

[9] Aharonian, F. *Very High Energy Cosmic Gamma Radiation: A Crucial Window on the Extreme Universe*. World Scientific Publishing, Singapore, 2004.

[10] Aharonian, F., et al. H.E.S.S. observations of PKS 2155-304. *Astron. Astrophys.430* (Feb. 2005), 865–875.

[11] Aharonian, F., et al. Fast Variability of Tera-Electron Volt γ Rays from the Radio Galaxy M87. *Science 314* (Dec. 2006), 1424–1427.

[12] Aharonian, F., et al. Observations of the Crab nebula with HESS. *Astron. Astrophys.457* (Oct. 2006), 899–915.

[13] Aharonian, F., et al. Discovery of Very High Energy γ-Ray Emission from Centaurus a with H.E.S.S. *Astrophys. J., Letters695* (Apr. 2009), L40–L44.

[14] Aharonian, F., Konopelko, A. K., Völk, H. J., and Quintana, H. 5@5 - a 5 GeV energy threshold array of imaging atmospheric Cherenkov telescopes at 5 km altitude. *Astroparticle Physics 15* (Aug. 2001), 335–356.

[15] Akhperjanian, A., and Sahakian, V. Performance of a 20 m diameter Cherenkov imaging telescope. *Astroparticle Physics 21* (May 2004), 149–161.

[16] Axford, W. I., Leer, E., and Skadron, G. The acceleration of cosmic rays by shock waves. In *International Cosmic Ray Conference* (1977), vol. 11 of *International Cosmic Ray Conference*, pp. 132–137.

[17] Bauleo, P. M., and Rodríguez Martino, J. The dawn of the particle astronomy era in ultra-high-energy cosmic rays. *Nature458* (Apr. 2009), 847–851.

[18] Bell, A. R. The acceleration of cosmic rays in shock fronts. I. *Mon. Not. Roy. Astron. Soc.182* (Jan. 1978), 147–156.

[19] Berge, D. *A detailed study of the gamma-ray supernova remnant RX J1713.7-3946 with H.E.S.S.* PhD thesis, Ruperto-Carola University of Heidelberg, Germany, 2006.

[20] Bernlöhr, K. *CORSIKA and sim_telarray – Simulation of the imaging atmospheric Cherenkov technique*, September 2012.

[21] Bernlöhr, K., et al. Monte Carlo design studies for the Cherenkov Telescope Array. *ArXiv e-prints* (Oct. 2012).

[22] Cappellari, M., Neumayer, N., Reunanen, J., van der Werf, P. P., de Zeeuw, P. T., and Rix, H.-W. The mass of the black hole in Centaurus A from SINFONI AO-assisted integral-field observations of stellar kinematics. *Mon. Not. Roy. Astron. Soc.394* (Apr. 2009), 660–674.

[23] Fermi, E. On the Origin of the Cosmic Radiation. *Physical Review 75* (Apr. 1949), 1169–1174.

[24] Gaisser, T. K. *Cosmic Rays and Particle Physics*. Cambridge University Press, Cambridge, 1990.

[25] Hanlon, W. `http://www.physics.utah.edu/~whanlon/spectrum.html`. 15. 3. 2013.

[26] Heck, D., Knapp, J., Capdevielle, J. N., Schatz, G., and Thouw, T. *CORSIKA: a Monte Carlo code to simulate extensive air showers.* Forschungszentrum Karlsruhe GmbH, Karlsruhe, Germany, 1998.

[27] Heck, D., and Pierog, T. *Extensive Air Shower Simulation with CORSIKA: A User's Guide (Version 6.990)*, July 2012.

[28] Hess, V. Über Beobachtungen der durchdringenden Strahlung bei sieben Freiballonfahrten. *Physik. Z. 10* (1912), 1084.

[29] Hillas, A. M. The Origin of Ultra-High-Energy Cosmic Rays. *Ann. Rev. of Astron. & Astroph.22* (1984), 425–444.

[30] Hillas, A. M. Differences between Gamma-Ray and Hadronic Showers. In *TeV Gamma-ray Astrophysics. Theory and Observations* (1996), H. J. Voelk and F. A. Aharonian, Eds., pp. 17–30.

[31] Hinton, J. Ground-based gamma-ray astronomy with Cherenkov telescopes. *New Journal of Physics 11*, 5 (May 2009), 055005.

[32] Horiuchi, S., Meier, D. L., Preston, R. A., and Tingay, S. J. Ten Milliparsec-Scale Structure of the Nucleus Region in Centaurus A. *Pub. Astron. Soc. Japan58* (Apr. 2006), 211–216.

[33] Israel, F. P. Centaurus A - NGC 5128. *Astron. Astrophys. Rev.8* (1998), 237–278.

[34] Joshi, J. C., and Gupta, N. Testing hadronic models of gamma ray production at the core of Cen A. *Phys. Rev. D87*, 2 (Jan. 2013), 023002.

[35] Kachelriess, M. Lecture notes on high energy cosmic rays. *ArXiv e-prints* (Jan. 2008).

[36] Konopelko, A., Aharonian, F., Hemberger, M., Hofmann, W., Kettler, J., Pühlhofer, G., and Völk, H. J. Effectiveness of TeV γ-ray observations at large zenith angles with a stereoscopic system of imaging atmospheric Cerenkov telescopes. *Journal of Physics G: Nuclear and Particle Physics 25* (Sept. 1999), 1989–2000.

[37] Lagage, P. O., and Cesarsky, C. J. The maximum energy of cosmic rays accelerated by supernova shocks. *Astron. Astrophys.125* (Sept. 1983), 249–257.

[38] Lenain, J.-P., Boisson, C., Sol, H., and Katarzyński, K. A synchrotron self-Compton scenario for the very high energy γ-ray emission of the radiogalaxy M 87. Unifying the TeV emission of blazars and other AGNs? *Astron. Astrophys.478* (Jan. 2008), 111–120.

[39] Li, T.-P., and Ma, Y.-Q. Analysis methods for results in gamma-ray astronomy. *Astrophys. J.272* (Sept. 1983), 317–324.

[40] Longair, M. S. *High Energy Astrophysics*. Cambridge University Press, Cambridge, 2011.

[41] Nedbal, D. Lecture notes on Cosmic Rays. 2011.

[42] Nedbal, D. *Search for High Energy Gamma Rays from Extragalactic Objects with H.E.S.S.* PhD thesis, Charles University, Prague, Czech Republic, 2009.

[43] Nosek, D. Private communications. 2013.

[44] Particle Data Group. Atomic and nuclear properties of materials. `http://pdg.lbl.gov/2012/AtomicNuclearProperties/HTML_PAGES/104.html`. 4. 4. 2013.

[45] Particle Data Group. Summary plot of hadronic p, γp, $\gamma\gamma$ total collision cross-sections. `http://pdg.lbl.gov/2012/hadronic-xsections/hadron.html`. 19. 3. 2013.

[46] Pesce-Rollins, M., and for the Fermi LAT collaboration. First results on Cosmic Ray electron spectrum below 20 GeV from the Fermi LAT. *ArXiv e-prints* (July 2009).

[47] Rosswog, S., and Brüggen, M. *Introduction to High Energy Astrophysics*. Cambridge University Press, Cambridge, 2007.

[48] Roustazadeh, P., and Böttcher, M. Very High Energy Gamma-ray-induced Pair Cascades in the Radiation Fields of Dust Tori of Active Galactic Nuclei: Application to Cen A. *Astrophys. J.728* (Feb. 2011), 134.

[49] Sahakian, V., Aharonian, F., and Akhperjanian, A. Cherenkov light in electron-induced air showers. *Astroparticle Physics 25* (May 2006), 233–241.

[50] Sahakyan, N., Yang, R., Aharonian, F., and Rieger, F. M. Evidence for a second component in the high-energy core emission from Centaurus A? *Astrophys. J., Letters* (submitted for publication, 2013).

[51] Sahu, S., Zhang, B., and Fraija, N. Hadronic-origin TeV γ rays and ultrahigh energy cosmic rays from Centaurus A. *Phys. Rev. D85*, 4 (Feb. 2012), 043012.

[52] Stanev, T. *High Energy Cosmic Rays*. Springer, 2004.

[53] Stawarz, Ł., Aharonian, F., Wagner, S., and Ostrowski, M. Absorption of nuclear γ-rays on the starlight radiation in FR I sources: the case of Centaurus A. *Mon. Not. Roy. Astron. Soc.371* (Oct. 2006), 1705–1716.

[54] Szanecki, M., Bernlöhr, K., Sobczyńska, D., Niedźwiecki, A., Sitarek, J., and Bednarek, W. Influence of the Geomagnetic Field on the IACT detection technique for possible sites of CTA observatories. *ArXiv e-prints* (Feb. 2013).

[55] Štefánik, S. *Studium kosmického gama záření*. Bachelor thesis, Charles University, Prague, Czech Republic, 2011.

[56] Wakely, S., and Horan, D. TeVCat, an online gamma-ray catalog. `http://tevcat.uchicago.edu/`. 5. 3. 2013.

List of Figures

List of Abbreviations

AGN - active galactic nucleus

Cen A - Centaurus A

CMB - cosmic microwave background

CR - cosmic rays

CTA - Cherenkov Telescope Array

GZK - Greisen-Zatsepin-Kuzmin (cutoff)

H.E.S.S. - High Energy Stereoscopic System

IACT - imaging atmospheric Cherenkov technique/telescope

IC - inverse Compton (scattering)

MRSW/MRSL - mean reduced scaled width/length

PAO - Pierre Auger Observatory

PSF - point spread function

SED - spectral energy distribution

SNR - supernova remnant

SSC - synchrotron self-Compton (model)

VHE - very high energy

UHECR - ultra high energy cosmic rays